

TESS Planet Occurrence Rates Reveal the Disappearance of the Radius Valley Around Mid-to-Late M Dwarfs

ERIK DIEGO GILLIS ¹, RYAN CLOUTIER ¹ AND EMILY K. PASS ^{2,*}

¹*Department of Physics & Astronomy, McMaster University, 1280 Main St West, Hamilton, ON, L8S 4L8, Canada*

²*Kavli Institute for Astrophysics and Space Research, Massachusetts Institute of Technology, Cambridge, MA 02139, USA*

(Revised February 26, 2026)

Submitted to Submitted to AAS Journals

ABSTRACT

We present the deepest systematic search for planets around mid-to-late M dwarfs to date. We have surveyed 8134 mid-to-late M dwarfs observed by TESS with a custom built pipeline and recover 77 vetted transiting planet candidates. We characterize the sensitivity of our survey via injection–recovery and measure the occurrence rate of planets as a function of orbital period, instellation, and planet radius. We measure a cumulative occurrence rate of 1.10 ± 0.16 planets per star with radii $> 1 R_{\oplus}$ orbiting within 30 days. This value is consistent with the cumulative occurrence rate around early M dwarfs, making M dwarfs collectively the most prolific hosts of small close-in planets. Unlike the bimodal Radius Valley exhibited by close-in planet population around FGK and early M dwarfs, we recover a unimodal planet radius distribution peaking at $1.25 \pm 0.05 R_{\oplus}$. We additionally find 0.954 ± 0.147 super-Earths and 0.148 ± 0.045 sub-Neptunes per star, with super-Earths outnumbering sub-Neptunes 5.5:1, firmly demonstrating that the Radius Valley disappears around the lowest mass stars. The dearth of sub-Neptunes around mid-to-late M dwarfs is consistent with predictions from water-rich pebble accretion models that predict a fading Radius Valley with decreasing stellar mass. Our results support the emerging idea that the sub-Neptune population around M dwarfs is composed of water-rich worlds. We find no hot Jupiters in our survey and set an upper limit of 0.012 hot Jupiters per mid-to-late M dwarf within 10 days.

Keywords: Exoplanet astronomy (486), Exoplanet formation (492) M Dwarf Stars (982), Transit Photometry (1709), Astrostatistics (1882)

1. INTRODUCTION

The exoplanet community has recently surpassed the discovery of over 6000 exoplanets. This collection is mostly comprised from thousands of exoplanets uncovered by large-scale transit surveys, which have revolutionized our understanding of the planet population. The bulk of confirmed transiting planets have been discovered by the Kepler space telescope, which has provided a clear picture of the rates of close-in planets around FGK and early M type stars (A. W. Howard et al. 2012; C. D. Dressing & D. Charbonneau 2015; B. J. Fulton et al. 2017; R. Cloutier & K. Menou 2020).

Despite Kepler’s unprecedented and significant contributions, the telescope’s focus on a single field and relatively blue bandpass (420-900 nm; D. G. Koch et al. 2010) limited Kepler’s ability to provide detailed characterization of the planet population around mid-to-late M dwarfs due to their red spectra. These stars have $\lesssim 0.4 R_{\odot}$, and represent the most common type of star in the galaxy (J. G. Winters et al. 2015). Previous works have provided constraints on the cumulative sub-Neptune and super-Earth occurrence rates around mid-to-late M dwarfs using data from Kepler and K2 (K. K. Hardegree-Ullman et al. 2019, 2025), but a more detailed characterization of the planet population around these remains limited with Kepler.

In 2018, the Transiting Exoplanet Survey Satellite (TESS; G. R. Ricker et al. 2015) launched. TESS is en-

Email: gillie1@mcmaster.ca

* Juan Carlos Torres Postdoctoral Fellow

abling the investigation of the planet population around mid-to-late M dwarfs in two key ways. Its large field-of-view and full sky access allows it to observe nearly every nearby mid-to-late M dwarf whereas Kepler and K2 were limited to roughly one thousand mid-to-late M dwarfs with stellar mass $< 0.4 M_{\odot}$. Additionally, TESS’s bandpass is significantly redder than Kepler’s (600-1000 nm), which improves the photometric precision by better covering the spectral energy distributions of these cool, red stars. This has enabled more detailed investigations into the occurrence rates of planets around the smallest stars, most recently by [K. Ment & D. Charbonneau \(2023, hereafter MC23\)](#) who characterized the exoplanet population around mid-to-late M dwarfs out to 7 days.

Kepler and TESS have provided a detailed window into the occurrence of planets with radii larger than Earth. This planet population around Sun-like stars ([B. J. Fulton et al. 2017](#)), late K and early M dwarfs alike ([R. Cloutier & K. Menou 2020, hereafter CM20](#)) is dominated by super-Earths and sub-Neptunes, with a dearth separating these two populations known as the Radius Valley. The ubiquity of this feature across spectral types has motivated the development of planet formation theories to explain the Radius Valley’s properties and the evolution of its features—most notably the slope separating the planet populations in period–radius space. Around FGK stars, thermally driven atmospheric escape through photoevaporation ([J. E. Owen & Y. Wu 2017](#)) and core-powered mass loss ([A. Gupta & H. E. Schlichting 2019](#)) have been shown to explain the Radius Valley’s properties. Conversely, there is a growing body of observational evidence that the Radius Valley around early M dwarfs is instead sculpted by the effects of water-rich formation and migration (e.g. [R. Cloutier & K. Menou 2020](#); [H. Diamond-Lowe et al. 2022](#); [R. Luque & E. Pallé 2022](#); [C. Cherubim et al. 2023](#); [C. Piaulet et al. 2023](#); [E. Gaidos et al. 2024](#); [C. S. K. Ho et al. 2024](#)). The planet population and any subsequent Radius Valley remains to be robustly characterized around the lowest mass main-sequence stars beyond planets orbiting within 7 days ([MC23](#)).

Here we present the results of a large-scale transit survey of 8134 mid-to-late M dwarfs with TESS to characterize the occurrence rates of terrestrial to Jovian-sized objects around mid-to-late M dwarfs. We survey our targets using a custom-built pipeline and employ detailed injection–recovery tests to characterize our survey’s sensitivity. By combining our sample of found planets with the completeness of our survey, we derive a robust understanding of the planet population around the most common stars.

Our paper is structured as follows: In [Section 2](#), we present our sample of stars, the cuts we apply to ensure that our sample is free from contamination, and our homogeneous stellar characterization. In [Section 3](#) we present our custom transit search pipeline to find and characterize transiting planets, along with the injection–recovery tests necessary to characterize our pipeline’s sensitivity. In [Section 4](#), we present our sample of recovered planets and in [Section 5](#) we combine this sample with the completeness of our survey to recover the occurrence rate of planets around mid-to-late M dwarfs out to 30 days. Finally, we present this work in context and highlight our conclusions with [Sections 6 and 7](#).

2. TARGET SAMPLE AND STELLAR CHARACTERIZATION

Our initial stellar sample for our survey follows from the targets proposed in TESS Guest Investigator (GI) Programs G03274³, G04214⁴, and G05152⁵. These programs aimed to characterize the demographics of the exoplanet population around mid-to-late M dwarfs to determine the dominant physical mechanism responsible for sculpting the Radius Valley in this stellar mass regime. The original survey sample requested 2-minute cadence light curves of 11,103 mid-to-late M dwarfs. Their target list comprised the set of known mid-to-late M dwarfs within 100 pc with mass $M < 0.45 M_{\odot}$ derived with the relation of [A. W. Mann et al. \(2019\)](#) and expected S/N > 7.3 for a fiducial transiting Radius Valley planet using the expected noise described in [P. W. Sullivan et al. \(2017\)](#). The mass cut in the initial target selection is conservative compared to the final mass cut in our survey, and the signal-to-noise cut effectively acts as a stellar radius dependent magnitude cut.

We begin by refining the original target list using updated astrometric and photometric observations from Gaia DR3. We retrieve the $G_{BP} - G_{RP}$ color, parallax, Gaia G magnitude and the Renormalised Unit Weight Error (RUWE) of each source observed by the aforementioned TESS GI programs. RUWE is a measure of the quality of a star’s astrometric fit in Gaia assuming that it is a single star. A high RUWE is characteristic of unresolved binary systems, and we reject any targets with $RUWE > 2.5$ because we cannot reliably derive

³ TESS Cycle 3, *Understanding The Physical Origin Of The Rocky/Non-Rocky Transition Around Mid-To-Late M Dwarfs With TESS*, PI: Cloutier.

⁴ TESS Cycle 4, *The Physical Origin of the Rocky/Enveloped Transition Around Mid-To-Late M Dwarfs*, PI: Cloutier.

⁵ TESS Cycle 5, *Establishing The Physical Origin of the Rocky/Enveloped Transition Around Mid-To-Late M Dwarfs with TESS*, PI: Cloutier.

stellar (nor planetary) parameters for unresolved binary systems. We retrieve each target’s 2MASS apparent K_s magnitude, and derive the Absolute K_s Magnitude (M_{K_s}) using its Gaia parallax and the distance modulus. We then attempt to remove white dwarfs and over-luminous sources from the sample using the main sequence in the $G_{BP} - G_{RP} / M_{K_s}$ color-magnitude diagram (see Figure 1). We reject all targets with a $G_{BP} - G_{RP}$ color more than 2.5 standard deviations away from the median per M_{K_s} . This cut preserves all confirmed planets and known TESS Objects of Interest (TOI) in this sample, which are transiting planet candidate signals identified by the TESS Science Processing and Operations Center (SPOC).

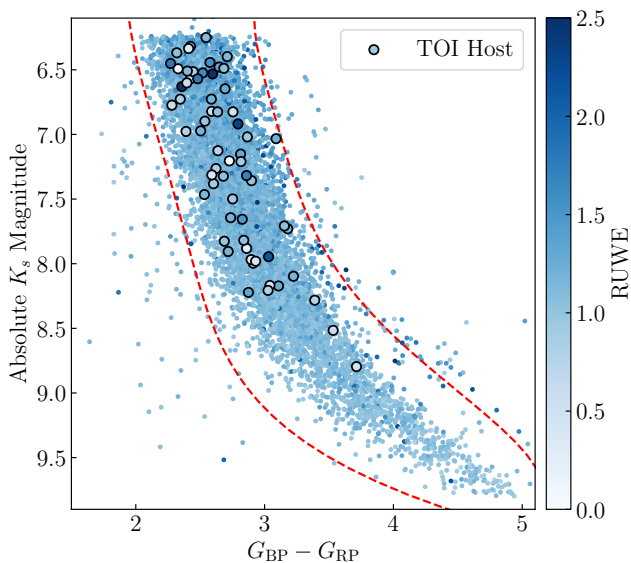


Figure 1. $M_{K_s} / G_{BP} - G_{RP}$ color-magnitude diagram of our original target sample, with color cuts plotted with the red dashed lines. Targets hosting TOIs are encircled.

Next, we derive stellar parameters for all remaining stars in our refined sample. We retrieve each star’s TESS magnitude (T_{mag}) and apparent K_s from the TIC. We calculate the stellar radii of each star using the empirically calibrated radius- K_s -band luminosity relationship for M dwarfs from A. W. Mann et al. (2015) and the mass of each target using the empirically calibrated mass- M_{K_s} -band luminosity relationship for M dwarfs from A. W. Mann et al. (2019). We retain all targets $M_{K_s} > 6.25$, corresponding to all M stars less massive than $0.4 M_{\odot}$, concretely focusing our survey on mid-to-late M dwarfs. This cut implicitly removes any giant M stars. These cuts in mass, color and RUWE leave 8134 mid-to-late M dwarfs for our survey.

We calculate the bolometric luminosities of our targets using two bolometric corrections from the K_s -band

and V-band respectively. For both methods, we begin by estimating the V-band magnitude using the $G - V - G_{BP} - G_{RP}$ color relations from D. W. Evans et al. (2018). We then compute a V-band bolometric correction BC_V using the $V - K$ color/V-band bolometric correction relationship provided by M. J. Pecaut & E. E. Mamajek (2013). This V-band bolometric correction, and our calculated V-band magnitude provides our first bolometric luminosity estimate using

$$L_{\text{bol}}/L_{\odot} = 10^{-0.4(M_V - BC_V - 4.74)}, \quad (1)$$

where 4.74 is the Sun’s absolute bolometric magnitude. We derive a second bolometric correction with the K_s -band magnitude, computing the bolometric correction in the K band from the $V - K_s - K_s$ -band bolometric correction provided in A. W. Mann et al. (2015). This K_s band bolometric correction and the observed K_s band magnitude provides our second bolometric luminosity estimate as in equation 1. The bolometric luminosities derived through the V-band magnitude is typically 6% higher than the bolometric luminosity calculated by through the K_s -band magnitude. We adopt the average of the two L_{bol} values as the star’s bolometric luminosity which have a typical error of 3%. We combine the computed radii with the derived L_{bol} values to calculate the effective temperature through the Stefan-Boltzmann law.

The distributions of T_{mag} , distance, effective temperature and mass and radius are plotted in Figure 2 with their respective medians marked.

3. TRANSIT SEARCH PIPELINE

3.1. Light Curve Data

We conduct our transit survey using all available TESS data for each of our targets from sectors 1 through 86 spanning six years of observation from July 25 2018 to December 18 2024. TESS images the sky with four cameras spanning a total 24×96 square degree field-of-view, and each sector of observation spans an approximately 28 day long pointing of the telescope. TESS records the brightness of each target using Simple Aperture Photometry (SAP) using an aperture of pixels subtended by the star on TESS’s detector. SAP derives the flux from a target by summing the dark-subtracted, debiased pixels within the TESS predetermined photometric aperture. This flux is subject to instrumental variations which are corrected for in the Presearch Data Conditioning Corrected SAP (PDCSAP; J. C. Smith et al. 2012; M. C. Stumpe et al. 2012, 2014). The PDCSAP uses principal component analysis over all light curves from the detector to remove large-scale correlated variations exhibited in all the sources on the detector. The PDCSAP flux

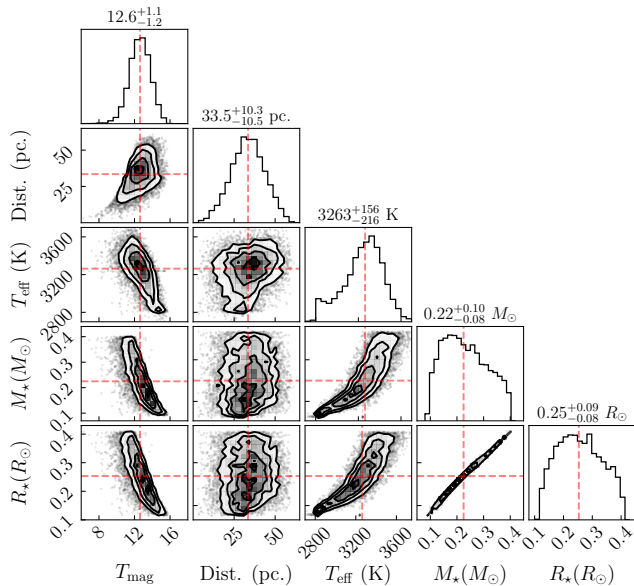


Figure 2. Distributions of T_{mag} , distance, effective temperatures, radii, masses and of our 8134 targets. The median of each column and row is marked with a dashed red line, which is also reported in the column titles along with each parameters’ 16th and 84th percentiles.

attempts to correct for large scale systematics while preserving sources of astrophysical variability in each target such as flares, transits, and stellar rotation signatures. For each sector in which a given target was observed, our pipeline retrieves the PDCSAP light curve and supplementary data products, which comprise the following timeseries: the BJD timestamp of each observation, the PDCSAP flux, the 1σ error on the PDCSAP flux, the exposure time, the data quality flags, and the sector of the observation. Any data with a nonzero quality flag (indicating some issue) are excised from the time series.

Our pipeline saves these data by concatenating sectors of consecutive observations as a series of light curves, up to a maximum of four consecutive sectors (~ 112 days). While a long baseline is ideal to detect shallow transits because many transits can be stacked to build S/N, the computational expense of a transit search scales exponentially with baseline duration, making transit searches of targets with many consecutive sectors of observation prohibitively expensive. Our imposed maximum light curve duration balances the sensitivity of our search over our period range with the computational expense of the pipeline employed to detect transit-like signals.

In our survey, we define our period search range of interest to span 0.2–30 days. The lower period limit of 0.2 days is motivated by the expected Roche limit for rocky planets around our target stars. The upper limit of our search is motivated by the number of targets with

at least two or more consecutive TESS sectors of observation, yielding at least one light curve of 56 days or longer. If we optimistically assume that the occurrence rate of planets at 30 days is 0.1, we ought to find 3 planets in our survey at 30 days if we have perfect sensitivity to transiting planets around the stars with 2 more consecutive sectors. The breakdown of targets with N consecutive sectors of observations is summarized in Table 1.

No. of Consecutive Sectors	Target Count (Fraction)
No Consecutive Sectors	4650 (57%)
Two Consecutive Sectors	2457 (30%)
Three Consecutive Sectors	648 (8%)
\geq Four Consecutive Sectors	379 (5%)

Table 1. Number of targets with observations in consecutive TESS sectors.

3.2. Cleaning and Detrending Light Curves

The methods we employ to find and characterize transiting planet candidates (PCs) with our pipeline are only reliable when run on light curves that have been cleaned of sporadic outliers, excess stellar variability, and residual systematics. Prior to our transit search, we clean each light curve following the methods described below.

Any data with a non-zero quality flag are excised from the time series. 76% of light curves have no flagged data, and in 95% of light curves, these flagged data comprise less than 0.1%. Mid-to-late M dwarfs are known to exhibit sporadic flaring events that we seek to identify and remove from our light curves. Our flare removal procedure follows S. W. Chang et al. (2015), where flares are identified by any sequence of three or more consecutive flux measurements that are three or more global median absolute deviations above the median of the light curve. When we detect these consecutive outliers are detected, the 30 data points on either side of the consecutive outliers are taken as part of the series which may contain the flare. With this sequence of data we apply the change-point algorithm described in S. W. Chang et al. (2015). With a sequence of flux measurements x_1, x_2, \dots, x_n with some mean \bar{x} we define the k^{th} cumulative sum as

$$S_k = \sum_{i=0}^k (x_i - \bar{x}). \quad (2)$$

A change-point corresponds to the maximum value of $|S_k|$ and its significance is determined by bootstrapping and comparing its value to the cumulative sum from shuffled x_i series. If its magnitude exceeds 90% of the

bootstrapped change-points, it is considered significant, and the series is divided into two sets on either side of the change-point. This process continues recursively on those subsets until no new change-points are identified. Identifying these change-points allows the pipeline to identify the extent of a flare. The identified change-points, along with the data in between them, are excised from the timeseries.

Many of our targets show strong quasi-periodic variation due to stellar rotational signals. In cases where this rotation signal is significant, we use a Gaussian process to remove the variation. We begin characterizing the rotation signal by computing the generalized Lomb-Scargle periodogram of each light curve (S. Schröter et al. 2019) to identify the best-fit sinusoid with a period of P_{GLS} , where $0.1 \text{ days} < P_{\text{GLS}} < T/2$ and T as the baseline of the light curve. To test whether the periodic signal is significant we perform a model comparison between this sinusoidal model and a constant flux model equal to the median of the light curve. We compare these two models using the Bayesian Information Criterion

$$\text{BIC} = -2 \ln(\mathcal{L}) + k \ln(n), \quad (3)$$

where \mathcal{L} is the likelihood of a model, k is the number of free parameters in the model (3 and 1 for the sinusoidal and constant models respectively), and n is the number of data points. The difference between the BICs for the sinusoidal and constant flux models quantifies how well one fits over the other and is expressed as the ΔBIC . We consider a periodic signal to be significant if the ΔBIC test favors the sinusoidal model by a score of 50 or more. Additionally, for light curves that exhibit rotational signals with $P_{\text{GLS}} > 1$ day, we also require that the amplitude of the rotation signal is greater than the median absolute deviation (MAD) of the light curve. The latter condition for longer period light curves is necessary because while Gaussian processes are efficient in removing rotation signals, they are also known to degrade transit signals (L. J. Garcia et al. 2024). We are able to characterize this effect using our injection–recovery tests, and outline the dilution in section 3.5. Out of our 8134 targets, 1,586 show significant signs of rotation according to this criterion. Since we require light curves with periods longer than 1 day to show greater amplitude modulation than the MAD of the light curve, our fraction of rotating targets (16%) is smaller than the fraction of rotating targets found by MC23 in their sample of mid-to-late M dwarfs.

Light curves without a significant rotational signal do not require a quasi-periodic model to detrend any rotational variability. We detrend these light curves using a running median filter with a 12-hour window. Each

light curve with significant rotation is detrended using a Gaussian process. Our Gaussian process (GP) employs the rotation term kernel provided by `celerite2` (D. Foreman-Mackey 2018). This kernel is a combination of two simple harmonic oscillator kernels, with two modes in Fourier space: one at the recovered rotation period given by the peak of the GLS periodogram, and one at one-half the recovered rotation period. The power spectral density of the simple harmonic oscillator is

$$S(\omega) = \sqrt{\frac{\pi}{2}} \frac{S_0 \omega_0^4}{(\omega^2 - \omega_0^2)^2 + \omega^2 \omega_0^2 / Q^2}, \quad (4)$$

where $\omega_0 = 1/P_{\text{GLS}}$ is the undamped angular frequency, Q is the quality factor, and S_0 characterizes the power at ω_0^2 . The parameters used in this model are further detailed in Table 2. The rotation term kernel combines two harmonic oscillators as $R(\omega) = S_1(\omega) + S_2(\omega)$. The respective parameters of S_1 and S_2 are

$$Q_1 = 1/2 + Q_0 + \Delta Q \quad (5)$$

$$\omega_{0,1} = \frac{4\pi Q_1}{P\sqrt{4Q_1^2 - 1}} \quad (6)$$

$$S_{0,1} = \frac{\sigma^2}{(1+f)\omega_{0,1}Q_1} \quad (7)$$

and

$$Q_2 = 1/2 + Q_0 \quad (8)$$

$$\omega_{0,2} = \frac{8\pi Q_2}{P\sqrt{4Q_2^2 - 1}} \quad (9)$$

$$S_{0,2} = \frac{f\sigma^2}{(1+f)\omega_{0,2}Q_2}. \quad (10)$$

The free parameters in Eqs. 5–10 are the hyperparameters of the rotation term kernel, and are outlined in Table 2.

3.3. Transiting Planet Search

We search for periodic transit-like signals in our detrended light curves using the Transit Least Squares algorithm (TLS; M. Hippke & R. Heller 2019a). TLS shares many similarities with the more traditional Box Least Squares (BLS; G. Kovács et al. 2002) algorithm, but instead of a boxcar function to fit transit-like signals, TLS fits a physically motivated transit model that incorporates the known stellar mass, radius, and quadratic limb-darkening coefficients to improve the signal-to-noise ratio of recovered signals and runtime efficiency. The TLS searches a range of transit periods, mid-transit epochs, and a set of transit durations, the latter of which

Gaussian Process Hyper-parameters:			
Parameter	Explanation	Prior	Unit
μ	Light curve mean	$\mathcal{N}(0, 10)$	Normalized Flux
$\log(\sigma_{\text{jitter}})$	Excess white noise	$\mathcal{U}(-3, 2)$	Normalized Flux
$\log(\sigma_{\text{gp}})$	GP Amplitude	$\mathcal{U}(-3, \log(\sigma_{\text{rms}}))$	Normalized Flux
σ_{lc}	Measurement uncertainty	$\log \mathcal{N}(\log(\bar{\sigma}), 0.1)$	Normalized Flux
P_{rot}	Rotation period	$\mathcal{N}(P_{\text{LS}}, 0.1)$	Days
Q_0	Quality factor	$\mathcal{N}(7.5, 2)$	Unitless
ΔQ	Difference between modes' quality factors	$\log \mathcal{N}(0, 1)$	Unitless
f	Secondary mode fractional amplitude	$\mathcal{U}(0.8, 1)$	Unitless

Planet Candidate Parameters and Priors:			
Parameter	Explanation	Prior	Unit
T_0	Mid-transit epoch of the final observed transit	$\mathcal{N}(T_{0,\text{TLS}}, \sigma T_{0,\text{TLS}})$	Days
P	Period of the transiting planet	$\mathcal{N}(P_{\text{TLS}}, \sigma P_{\text{TLS}})$	Days
R_p/R_\star	Planet-to-star radius ratio	$\log \mathcal{N}(0.005, 0.5)$	Unitless
b	Impact Parameters	$\mathcal{U}(0, 0.95)$	Unitless
F_0	Out of transit flux offset	$\mathcal{N}(0, \sigma_{\text{transit}})$	Normalized Flux

Table 2. Top: Summary of the parameters used in the Gaussian Process used to remove the strong stellar rotation signals from light curves. Here \mathcal{N} denotes a normal distribution, \mathcal{U} denotes a uniform distribution, $\log \mathcal{N}$ denotes a log-normal distribution, σ_{rms} is the standard-deviation of the light curve, P_{LS} is the period found by the Lomb-Scargle periodogram and $\bar{\sigma}$ is the median flux error. Bottom: Summary of parameters and priors used in the Monte-Carlo Markov chain used to fit planet parameters. Here, $T_{0,\text{TLS}}$ is the mid-transit epoch fit by the highest SDE TLS, $\sigma T_{0,\text{TLS}}$ is the uncertainty on $T_{0,\text{TLS}}$, P_{TLS} is the period found by the highest SDE TLS, σP_{TLS} is the uncertainty on P_{TLS} , and σ_{transit} is standard deviation of the light curve within two durations of the mid-transit.

encompasses all known exoplanets as of [M. Hippke & R. Heller \(2019a\)](#). TLS produces a signal detection efficiency (SDE) spectrum across a set of periods characterizing the goodness-of-fit of the best fit model marginalized over all other parameters. This process must be run iteratively to recover multi-planet systems in our sample. We identify transit-like signals from the TLS as periodicities with an SDE > 6 . We then run a least-squares optimization to fit a physical transit model using the `batman` ([L. Kreidberg 2015](#)) Python package to the TLS signal. The model is parameterized by the mid-transit epoch T_0 , the orbital period P , the planet-to-star radius ratio R_p/R_\star , the impact parameter b , and the quadratic limb-darkening parameters retrieved from the TIC. While the limb-darkening parameters could in principle be calculated manually given stellar parameters, any differences are expected to have a negligible effect on our model fits. We do not directly fit the transit parameter a/R_\star and instead calculate it from P , M_\star , and R_\star . We assume circular orbits by fixing the eccentricity to zero.⁶ We subtract the best fit model centered

at zero flux from the light curve to remove the detected signal. We continue this process iteratively until the TLS fails to find a signal with SDE > 6 or a maximum number of four iterations are run. We choose four iterations as our maximum because no targets in our sample have more than three confirmed planets or TOIs.

3.4. Planet Candidate Characterization

Each light curve yields a (possibly empty) set of transit candidate events (TCEs) and fit `batman` models. Each TCE must pass the following five vetting conditions:

1. The transit depth Δ from the best-fit transit model must result in a signal-to-noise ratio (S/N)

with zero for all but two planet candidates in our sample. Our fit planet parameters for all of our planet candidates are only negligibly affected. The two planet candidates for which we measure a non-zero eccentricities are LTT 3780 c (0.36 ± 0.16) and LP 261-75 C (0.38 ± 0.07). The former is known to have an orbit consistent with circular from joint transit and radial velocity fitting ([R. Cloutier et al. 2020](#)), and the latter is a known brown dwarf ([I. N. Reid & L. M. Walkowicz 2006](#)). This alternate model is only able to weakly constrain eccentricity for our other planet candidates with a typical 1σ upper limit of 0.36.

⁶ We ran preliminary tests with non-zero eccentricities and confirmed that the resulting eccentricity posteriors are consistent

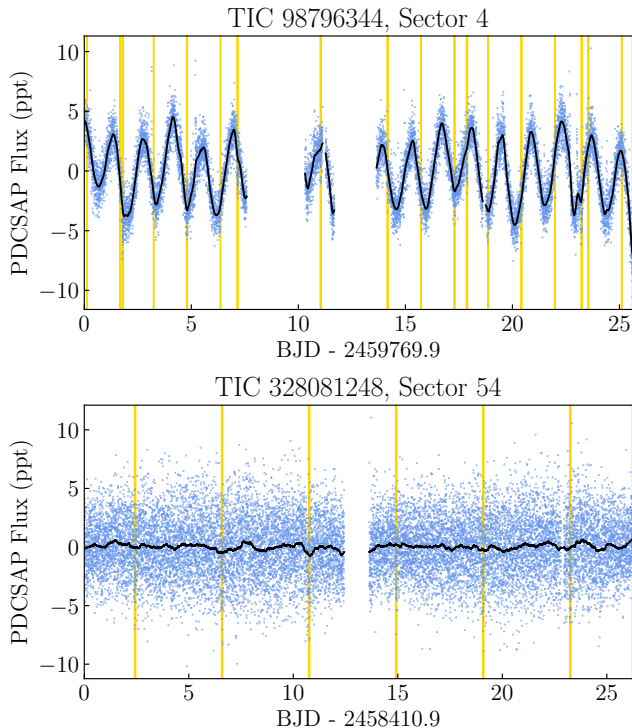


Figure 3. Selected light curves from TICs 98796344 (top) and 328081248 (bottom) respectively after flare removal. The trends recovered by a Gaussian process (top) and median filter (bottom) are overplotted in black, and the transit events in each light curve are highlighted in gold.

greater than 3. We define S/N as:

$$S/N = \frac{\Delta}{\sigma_{lc}} \sqrt{N_{\text{transits}}}, \quad (11)$$

where Δ is the TCE depth, N_{transits} is the number of transits observed, and σ_{lc} is the photometric rms of the light curve binned to the TCE’s duration.⁷ This intermediary cut does not represent the final S/N cutoff in our survey.

2. The period of the TCE cannot match the period of another higher S/N TCE from the same light curve within a tolerance of 0.1%.
3. The odd and even transit depths computed by the TLS must be consistent within 3σ .
4. The TLS result cannot have the same period, or be an integer multiple of the star’s rotation period

⁷ We note that σ_{lc} serves as proxy for the Combined Differential Photometric Precision (CDPP), which was only recently released by J. D. Twicken et al. (2025) and was not available at the time of our code development.

within a 0.3% tolerance. We note that this condition is only applicable to stars with strong evidence for rotation (see section 3.2). TLS results with $SDE > 15$ are exempt from this condition due to the significance of the result.

5. The TCE’s period must match the period of results from half the light curves or more, rounded down if the target has four or more light curves. TLS results with $SDE > 15$ and targets with ten or more sectors of observation are exempt from this condition.

We build a set of PCs by combining the TCEs with common properties from each light curve. Each of these PCs will be characterized by a joint fit using all available data at once, and further vetted with a second set of vetting conditions. From the sets of TCEs that our iterative search generates, we collect sets of TCEs with common depths within 20%, durations within 40%, and periods whose ratio is within 0.01% of an integer. Transit signals can be picked up as period aliases by the TLS motivating the need for a tolerance in period ratio rather than period, and the large ranges on durations and depth are necessary to account for these possibly misfolded signals.

To best characterize the PC’s period, we run a narrow TLS search within the period uncertainty of the result with the highest SDE using the full concatenated light curve. The pipeline then uses the folded light curve to fit the remaining transit parameters T_0 , R_p/R_* , b as well as an out of transit flux parameter F_0 to better characterize the transit baseline using `scipy.optimize.curve_fit` (P. Virtanen et al. 2020) with `batman` transit models.

At this stage, we require that the best-fit over all sectors of TESS data must have an $S/N > 6$. The pipeline further characterizes these PCs by running a Markov Chain Monte Carlo (MCMC) using the `emcee` package (D. Foreman-Mackey et al. 2013) to sample the posterior distributions of the five transit model parameters. These quantities and their respective priors are further outlined in Table 2. We also adopt quadratic limb-darkening parameters from the TIC as above.

To be considered a validated planet and therefore included in our forthcoming calculations of planet occurrence, each PC must pass a final set of statistical vetting conditions, which are calibrated to remove false alarms (i.e. statistical false positive signals that appear in the light curve and do not have an astrophysical origin) through searches of light curves without planet signals.

1. The five-parameter fit model must have a reduced χ^2 value of 1.5 or less.

2. A ΔBIC test must favor the fitted transit model over a flat line at the median of the folded light curve within 1 transit duration of the transit midpoint by -10 or more.
3. A second ΔBIC test must favor the fitted transit model over a flat line at F_0 within 1 transit duration of the transit midpoint by -10 or more.

To further protect our search from astrophysical false positives (i.e. non-transit astrophysical signals that mimic TCEs), we employ TRICERATOPS (S. Giacalone & C. D. Dressing 2020; S. Giacalone et al. 2021) which characterizes the likelihood that a given signal is an astrophysical false positive. TRICERATOPS conducts this analysis by considering all stars that might pollute the flux in the TESS photometric aperture, and compares the transit model to other phenomena which may produce periodic transit-like signals (e.g. background eclipsing binaries). We find that among the TOIs the pipeline is able to recover, none have a false positive probability (FPP) greater than 8%. In our survey, we choose to reject any signals with a TRICERATOPS FPP greater than 10%.

As an additional check for astrophysical FPs in our set of PCs, we search for evidence of in-transit centroid offsets, which are indicative of off-target transit-like signals or eclipsing binaries. We employ *exovetter* (S. Mullally et al. 2025) to this end, which compares the centroid of each in-transit event to the out-of-transit baseline to characterize the likelihood that the signal contributing to each transit is on target. Figure 4 illustrates an on-target and an off-target centroid from two PCs for our search. We reject signals with an on-target probability over all observed transits of $< 1\%$. We perform this analysis and the aforementioned TRICERATOPS vetting using the TESS full-frame images retrieved for the in- and out-of-transit epochs using *lightkurve* (Lightkurve Collaboration et al. 2018).

It bears mentioning that there has been extensive effort to validate PCs through the TESS Follow-up Observing Program (TFOP) by conducting strategic follow-up observations of many TOIs. While these data would certainly improve our ability to validate PCs found by our pipeline, these observations represent a heterogeneous dataset that cannot be consistently applied to all PCs. We therefore ignore the availability of any TFOP observations in our PC characterization and vetting.

3.5. Detection Sensitivity Characterization

We have run a suite of injection–recovery tests to characterize the detection sensitivity of our pipeline as a

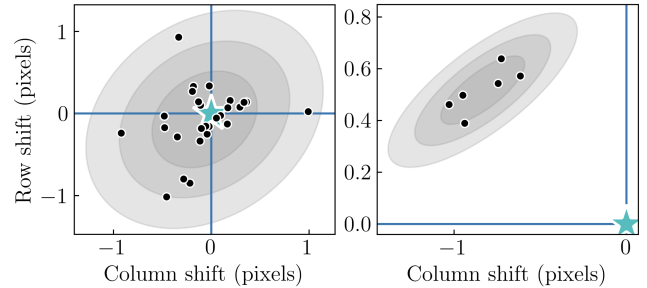


Figure 4. Example in-transit centroid offsets for TOIs 562.01 (left) and 3494.01 (right). The star marker in each panel marks the out-of-transit centroid and the black points mark the relative in-transit centroid positions of each TCE. The contours mark the 1, 2, and 3σ confidence intervals of the estimated in-transit centroid distribution. TOI-562.01 has a 97% on-target probability and TOI-3494.01 has a 0% on-target probability.

T_{mag}	Rotating?	Count (Fraction)
<12	Yes	366 (4.5%)
<12	No	2043 (25%)
12-13	Yes	402 (4.9%)
12-13	No	2261 (28%)
>13	Yes	562 (6.9%)
>13	No	2500 (31%)

Table 3. Target counts in each of our injection–recovery bins used to characterize our pipeline’s sensitivity.

function period and R_p/R_\star . Fully characterizing our pipeline’s sensitivity to transiting planets on a per-light curve basis is beyond the scope of the computational resources available for this project. Consequently, we consolidate this effort by calculating the average detection sensitivity within six sample bins. First targets were separated based on their magnitude with bins of $T_{\text{mag}} < 12$, 12–13 and > 13 respectively, with T_{mag} each bin containing roughly one third of our full sample. With this subdivision of our sample in T_{mag} , we aim to capture nonlinearities in photometric noise as a function of target brightness. We further subdivide these three magnitude bins into rotating and non-rotating subsamples based on the rotation criteria used in our pipeline. Rotating and non-rotating targets must be treated separately because the two different detrending methods used may introduce different noise properties in the resulting detrended light curves. The target counts in these bins are summarized in Table 3.

We inject signals with periods spanning 0.2–30 days, and injected R_p/R_\star from 0.01–0.2. The sampled period range corresponds to a R_p range of 0.3–5.5 R_\oplus around

an average star in our sample. These signals are forward modeled using `batman` and injected into the PD-CSAP light curve of a sampled target from the magnitude/rotation class bin under consideration. We inject this transit signal into the light curve of a randomly sampled target from the bin, before the light curve is processed in any way by our pipeline. Prior to injection any known TOI signals are masked using white noise matching the mean, local slope and scatter of the light curve at each transit epoch. We run our full transit search and claim a successful recovery of an injected signal if our transit search pipeline recovers a vetted PC whose recovered period P' matches any of: the injected period P , Pn , or P/n where $n \in \{2, 3, 4, 5, 6\}$ within a tolerance of 0.2%.

Our strategy to efficiently sample the period- R_p/R_* parameter space with injections follows `MC23` over the period- R_p/R_* space. The space is initially sectioned into four leaves using a quadtree, with a minimum 50 injections in each leaf of the tree. Within each leaf, P and R_p/R_* values are sampled from log-uniform distributions, with T_0 and b drawn uniformly from 0- P and 0-1, respectively. Once each leaf of the tree is populated with at least 50 injections, we determine whether more injections are required to accurately resolve the space. If two neighboring leaves of the tree in $P - R_p/R_*$ space differ in cumulative recovery rate by more than 15%, we recurse into the leaf by rebinning the leaf into four smaller leaves. We perform a maximum of five recursions with this method.

Our injection-recovery maps for each of the six bins considered are depicted in Figure 5. In comparing our rotating versus non-rotating TESS magnitude bins, we find worse sensitivity for shallow signals as TESS magnitude increases. We also see a sharp falloff beyond 14-day periods over all bins. This is expected, as 4,650 of our targets lack any consecutive sectors of observations, which makes detecting planets with orbital periods >14 days impossible. We also see that our pipeline's sensitivity is degraded around rotating stars compared to non-rotating stars of the same magnitude. This isn't unexpected, as Gaussian processes are known to degrade transit signals (L. J. Garcia et al. 2024). This drop in sensitivity may also indicate that active targets have a higher noise floor than non-active targets because active stars exhibit higher levels of uncorrelated jitter that cannot be removed through detrending.

Our injection-recovery tests also offer us insight into how reliable our detrending methods are in preserving the radius of injected planets by comparing the ratio of the injected radius to the recovered radius. Over our set of non-rotating targets where a median filter was used

in detrending, we find that $R_{p,\text{rec}}/R_{p,\text{inj}} = 0.96 \pm 0.05$. Over the set of rotating targets where a GP was used for detrending, we find that $R_{p,\text{rec}}/R_{p,\text{inj}} = 0.86^{+0.10}_{-0.20}$, which is not surprising because it is known that GPs can degrade transit depths (L. J. Garcia et al. 2024).

In Figure 6 we illustrate $R_{p,\text{rec}}/R_{p,\text{inj}}$ as a function of injected R_p/R_* for our median-detrended and GP-detrended samples along with their respective 1σ ranges. We clearly see that the degradation of the transit depth at our GP models is less impactful for small R_p/R_* . Considering transit injections into the light curves of rotating stars with $R_p/R_* < 0.05$ (corresponding to a radius of $1.2 R_\oplus$ around our median stellar radius of $0.25 R_\odot$), we find $R_{p,\text{rec}}/R_{p,\text{inj}} = 0.90^{+0.08}_{-0.12}$. We will revisit this effect in Section 4 and note that the degradation of the transit depths by our GP model does not have a strong effect on our planet sample due to the small fraction of found transiting planets orbiting stars that exhibiting rotation.

We convert the full sensitivity of our pipeline from period- R_p/R_* space to period- R_p space and instellation- R_p space as we are ultimately interested in characterizing planetary occurrence as a function of these quantities. We convert injected orbital period to instellation, spanning $1 - 1000 S_\oplus$, using the expression

$$S = S_\oplus \left(\frac{T_{\text{eff}}}{5777 \text{ K}} \right)^4 \left(\frac{P}{365.25 \text{ d}} \right)^{-\frac{4}{3}} \left(\frac{R_*}{R_\odot} \right)^2 \left(\frac{M_*}{M_\odot} \right)^{-\frac{2}{3}}. \quad (12)$$

Similarly, our converted planetary radii span $0.5 - 6.5 R_\oplus$. In our conversions, we use the calculated stellar parameters associated with each target.

Figure 7 depicts the resulting average detection sensitivity maps as functions of $P - R_p$ and $S - R_p$, respectively. These maps are computed from the weighted average of the six T_{mag} /rotation bin maps, where each contributing map is weighted by the fraction of our sample targets that fall within that bin. We note that because all injections have been transformed to radius and instellation spaces, dependent on the parameters of each target, the full extent of our sensitivity characterization can be extended beyond the ranges depicted in Figure 7. Our pipeline is sensitive to 50% of planets with $R_p = 1 R_\oplus$ out to 0.5 days and 50% of planets with $R_p = 2 R_\oplus$ out to 8 days. Our survey has limited sensitivity to sub-Earth-sized planets because of the wide range of targets' T_{mag} surveyed and the characteristic unsuitability of our faint targets to the detection of sub-Earths. We also have very limited sensitivity to planets within the habitable zone (HZ). For example, beyond a conservative inner HZ edge of $0.9 S_\oplus$ based on the water-loss limit (R. K. Kopparapu et al. 2013), we have 30% sensitivity to planets with $R_p = 3 R_\oplus$, which degrades to 12%

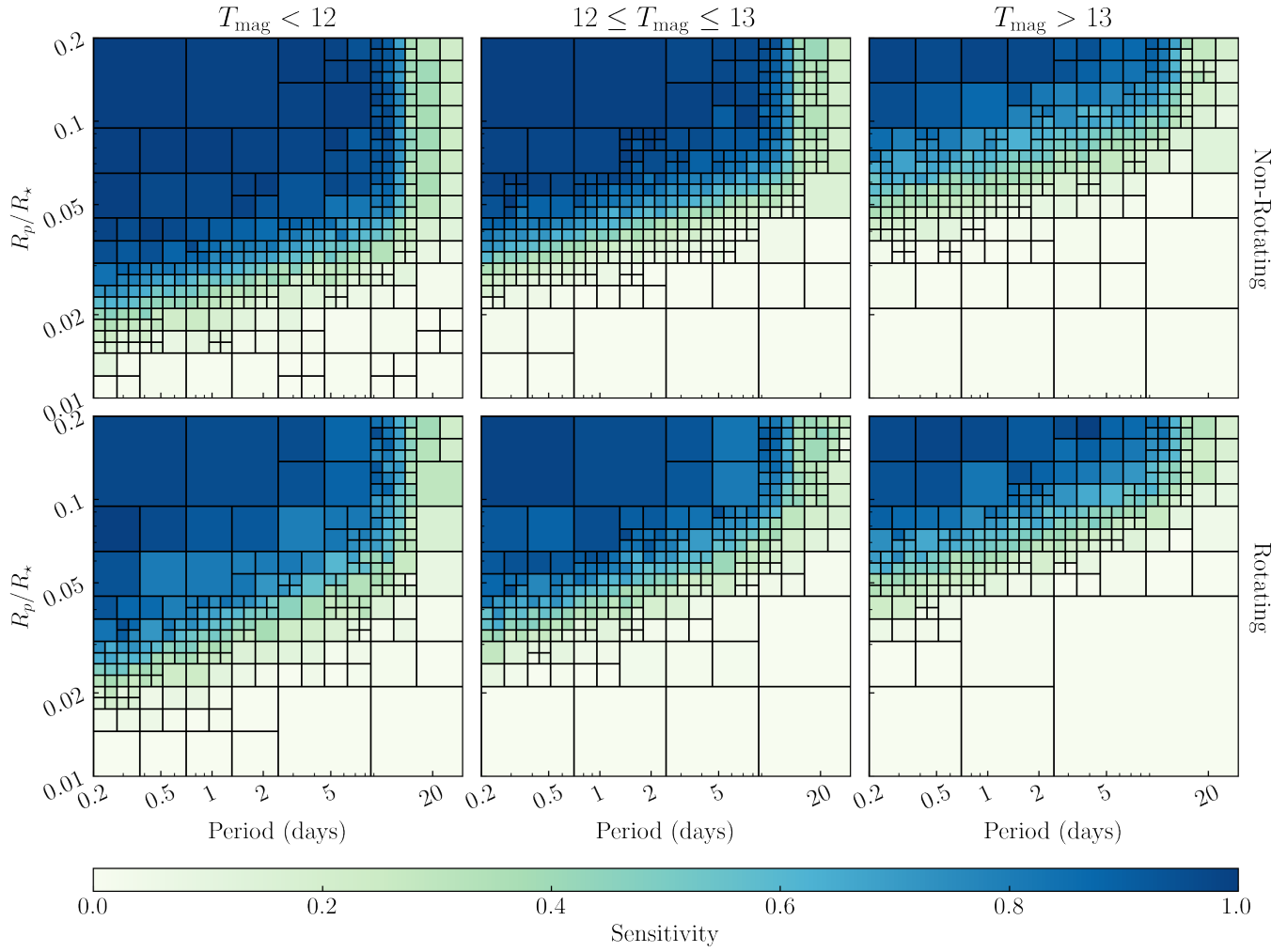


Figure 5. Injection/recovery maps over each of our six injection recovery target bins that span different TESS magnitudes (columns) and non-rotating (top row) and rotating targets (bottom row) showing our pipeline’s sensitivity to transiting planet signals across period– R_p/R_* space. Each cell in this recursive structure contains at least 50 injected planets with the black grid denoting the boundaries of each cell.

sensitivity for Earth-size planets. Our sensitivity drops steeply toward lower instellation values due to the fact that we only search out to a maximum period of 14 days for 57% of our targets with zero consecutive sectors of observation. These relatively poor sensitivity limits imply that we will only be positioned to make weak statements regarding the occurrence rate of sub-Earth and the population of HZ planets around mid-to-late M dwarfs. The low transit probability of relatively far out HZ planets compounds with our low sensitivity, making HZ planet detections exceedingly unlikely.

We note that our injection–recovery maps, when converted from R_p/R_* to R_p , do not extend to planets larger than $\sim 6.5 R_\oplus$. This being said, our survey sensitivity to these large planets is high ($> 93\%$) and appears roughly constant per orbital period. In Section 5 we will use this property of our sensitivity calculations to

extrapolate this high sensitivity to constrain the occurrence rate of close-in Jovian planets around mid-to-late M dwarfs.

3.6. Transit Survey Completeness

Occurrence rate inferences depend on the survey completeness, which is the product of the detection sensitivity computed from our injection–recovery tests and the geometric transit probability. For a given injected planet, we adopt a transit probability of

$$P_{\text{tr}} = \frac{R_\star}{a} \quad (13)$$

where a is the semi-major axis calculated from the planet’s orbital period and host star mass using Kepler’s third law. The transit probability is independent of the host star’s T_{mag} and rotation period such that we compute the average P_{tr} over our full sample of stars in the

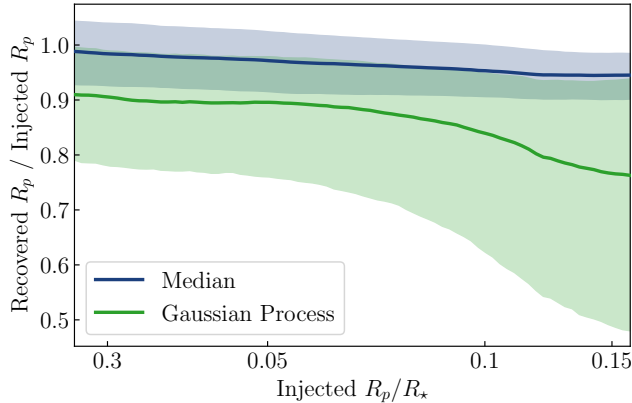


Figure 6. The ratio of recovered planet radii to injected planet radii as a function of the injected R_p/R_* injected. The curves depict the biases on our inferred planetary radii under our median filter (blue) and GP (green) detrending models. The shaded regions depict the $\pm 1\sigma$ intervals around each curve.

$P - R_p$ and $S - R_p$ parameter spaces. The product of our sample’s average transit probability and survey sensitivity (c.f. Figure 7) yields our survey completeness maps, which we denote as $c(P, R_p)$ and $c(S, R_p)$.

4. PLANET SEARCH RESULTS

Using our pipeline described in Section 3, we systematically search each of our 8134 targets for transiting planets from 0.2 to 30 days. Our pipeline identifies, vets, and subsequently characterizes TCEs that pass each of our vetting and statistical validation conditions.

TRICERATOPS and *exovetter* are incorporated into our vetting procedure to filter out probable false positives.

To converge on our final population of planets that can be used for occurrence rate calculations, our recovered set of PCs must be corrected for a non-zero false alarm rate to avoid overestimating occurrence rates. We note that our injection–recovery module is designed to calculate the false negative rate (i.e. detection sensitivity) but is not suited to characterizing the false alarm rate because only physical signals (i.e. true positives) are injected. We therefore inspect the PCs vetted by our fully automated transit search to attempt to identify and remove probable false alarms. This vetting step involves the detailed inspection of each PC’s TLS results, the pre- and post-detrending light curves, the phase-folded light curve and transit fit results from our MCMC analysis. Common false alarms include imperfect detrending of rotation signals and unflagged light curve edge effects. Following this step we proceed by assuming that our sample is free from false alarms.

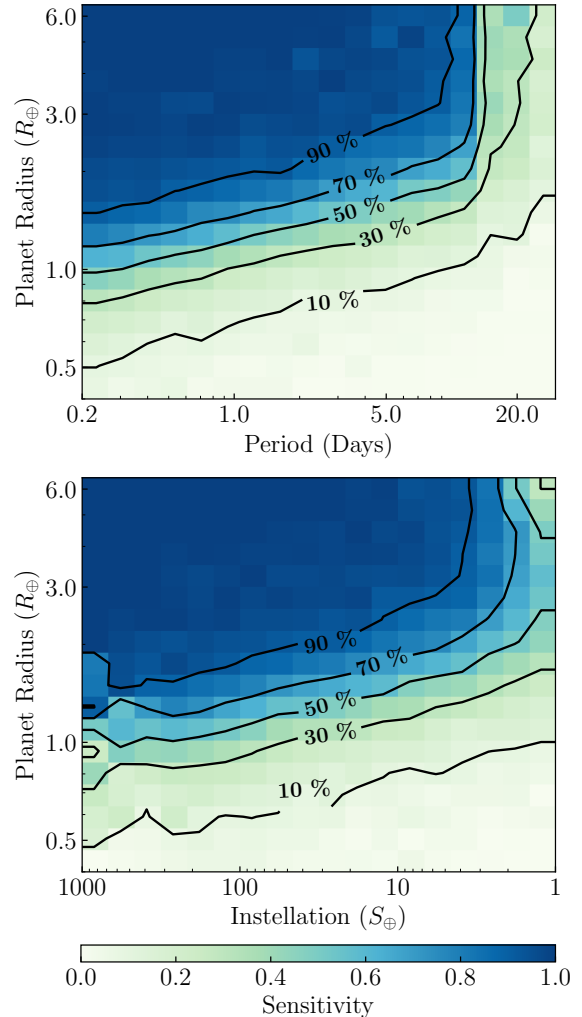


Figure 7. The average sensitivity of our survey as a function of period, planet radius, radius and instellation from 0.2 – 30 days, $0.5 - 6.5 R_\oplus$, and $1 - 1000 S_\oplus$, respectively.

Over our full set of survey targets, 532 TCEs are identified that pass our pipeline’s statistical vetting conditions. TRICERATOPS rejects 427 (80.2%) of these with an FPP $> 10\%$. Of the 105 remaining, *exovetter* rejects 5, and 23 are rejected by our manual vetting. After statistical and manual vetting, our pipeline recovers a total of 77 transiting PCs around 65 different stars. The periods, radii and instellations of these PCs are overplotted in Figure 8 (see Section 5.1). These PCs represent the set of planets that we will use to calculate planetary occurrence rates in Section 5. The remaining PC recovered by our pipeline is a newly discovered PC around TIC 149927512, which we detail below. Among these 77 PCs, 76 have transit parameters consistent with a corresponding TOIs.

Notably absent from our PC sample are planets with orbital periods between 20–30 days. According to the

NASA Exoplanet Archive queried on December 18 2025, there are six such confirmed transiting planets around mid-to-late M dwarfs. All but one of these planets’ host stars⁸ are absent from our stellar sample. The one exception is LHS 1140 (J. A. Dittmann et al. 2017; C. Cadieux et al. 2024), which hosts the sub-Neptune LHS 1140 b with a period of 24.7 days. LHS 1140 was observed by TESS in sectors 3 and 30, and as such it was not observed in consecutive sectors. By the design of our planet search, we can only detect planets out to 14 days in single sectors making LHS 1140 b undetectable. We note that we do detect LHS 1140 c (K. Ment et al. 2019).

Out of the 77 vetted PCs detected, only 10 are found around targets with strong signals of rotation where a GP was used to detrend the light curve. Additionally only two of these ten have $R_p/R_\star > 0.05$. Since these planets do not represent a significant fraction of our planet sample, and because we have established in Figure 6 that the detrimental impact of the GP on measured transit depth is relatively small ($\sim 10\%$ for $R_p/R_\star < 0.05$), we do not attempt to correct the recovered radii of planets detected in light curves detrended by a GP model.

Our full set of recovered planetary parameters is available in machine readable form and we present a subset of this table in Appendix A.

We detect a previously unidentified signal around TIC 149927512, which does not appear to have been previously identified as a known planet, a TOI, or a Community TOI (CTOI). This PC passes all of our vetting conditions. We recovered this transit-like signal around TIC 149927512 ($M_\star = 0.25 M_\odot$, $R_\star = 0.27 R_\odot$, $T_{\text{eff}} = 3269$ K) with an orbital period of $P = 1.4646834^{+0.0000028}_{-0.0000024}$ days and a radius of $R_p = 0.917^{+0.070}_{-0.067} R_\oplus$. TIC 149927512 was observed by TESS in sectors 14, 21, 41, 48, 74 and 75, and we detected the planet candidate in the TLS results of sector 21 and the combined sectors 74 and 75. The corresponding in-transit centroid offsets, TLS results, PDCSAP light curves, phase-folded light curve with fitted transit model, and transiting planet parameters are outlined in Appendix B. We note that the inclusion or omission of this PC in our subsequent occurrence rate calculation does not significantly impact our derived occurrence rates.

⁸ TRAPPIST-1 h (M. Gillon et al. 2017), Kepler-1512 b (G. Torres et al. 2017), Kepler-54 d (C. D. Dressing & D. Charbonneau 2013), K2-72 e (I. J. M. Crossfield et al. 2016), TOI-1227 b (A. W. Mann et al. 2022).

4.1. Comparison to known TOIs

To complement the detailed characterization of our pipeline’s detection sensitivity via injection–recovery tests (see Section 3.5), here we assess the recovery rate of known TOIs in our survey sample. Figure 9 depicts the sample of TOIs in our survey sample as of October 2024 that have not been vetted as false alarms or false positives, and includes confirmed/known planets as well as TOIs whose dispositions remain as PCs. The set of recovered TOIs have a median S/N of 12.98 and a minimum S/N of 6.76 (TOI 6258.01). We note that our pipeline finds and accurately characterizes all 36 confirmed planets in our sample and 74/80 (93%) of all TOIs (including confirmed planets) in our sample as of October 2024.

Here we detail why our pipeline fails to recover six TOIs, each of which are currently considered to be non-confirmed (i.e. planet candidates) and therefore may ultimately be revealed to be false positives. Our pipeline rejects TOI-3494.01 (S/N 10.7 at 7.74 days) during vetting due to the in-transit centroids showing a systematic offset from the target and an on-target probability of less than 1%. We therefore interpret TOI-3494.01 as a probable false positive. TOIs 2495.01, 5716.01, 6002.01, 6714.01, and 6716.01 were likely missed by our pipeline because our TLS searches did not produce any TCEs with periods that closely match the TOIs. All of these signals exhibit a low transit S/N < 8 . These TOIs may have been missed by our pipeline because unlike the TESS Transiting Planet Search (TPS; J. M. Jenkins 2002; J. M. Jenkins et al. 2010), we did not conduct our transit search over all available TESS data simultaneously due to runtime limitations, which limits our ability to recover low S/N signals.

5. OCCURRENCE RATE CALCULATION

5.1. Planetary Occurrence versus Planet Radius, Orbital Period, and Instellation

We calculate the planetary occurrence rate distribution over planet radius–period space and planet radius–instellation space, denoted $f(P, R_P)$ and $f(S, R_P)$, respectively. We bin these parameter spaces into discrete grids to calculate the cumulative occurrence rate within each grid cell. Following C. D. Dressing & D. Charbonneau (2015, hereafter DC15), we measure the occurrence rate in each cell as a binomial distribution. This follows from the view that the occurrence rate measurement in each bin is the result of a Bernoulli experiment whose probability of success depends on the product of the occurrence rate f and completeness c . For brevity, and without loss of generality, we outline the computation

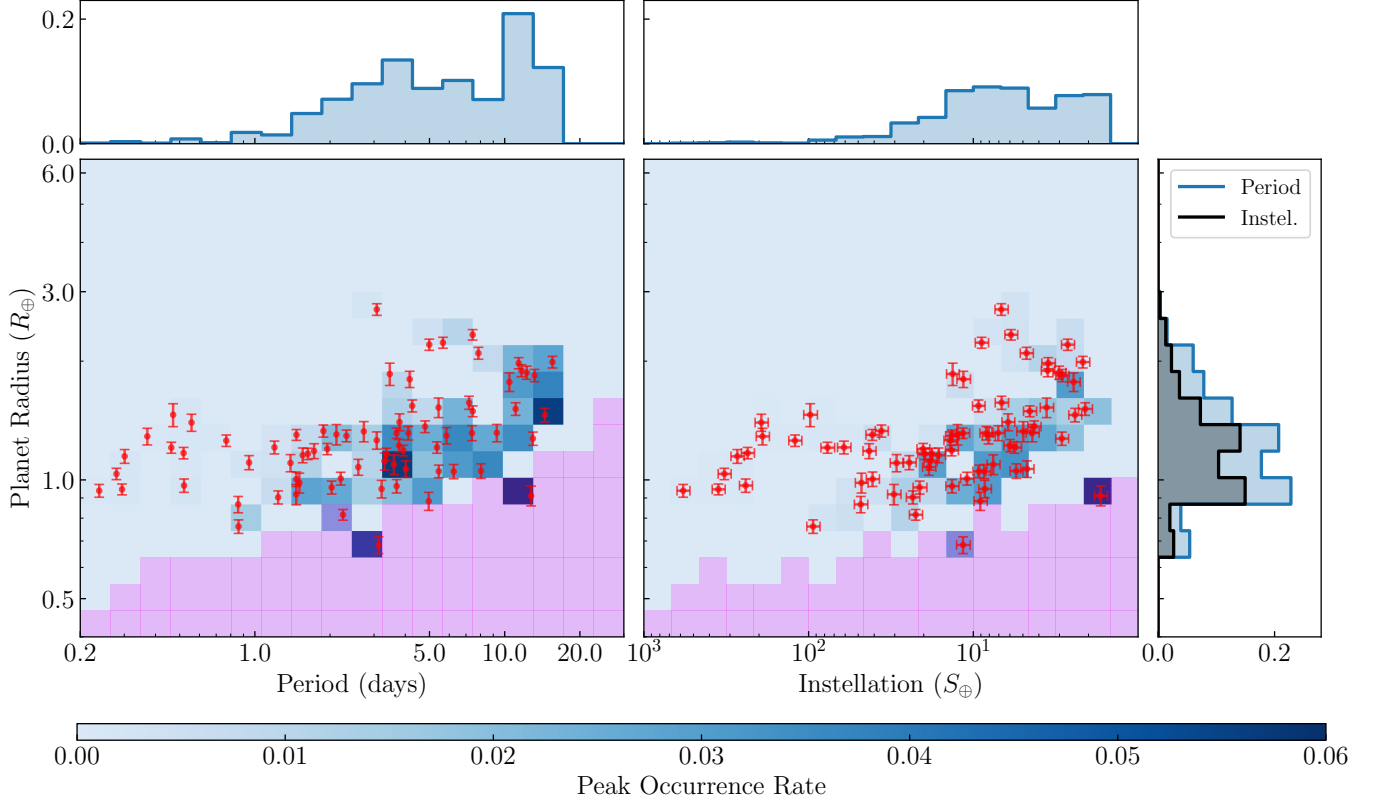


Figure 8. Distribution of our found planets in period–radius space (left) and instellation–radius space (right). Each planet and its associated errors are marked with the red points, while the background grid shows the peak occurrence rate f_{peak} in each bin of the grid. Regions where our average sensitivity is $< 10\%$ are highlighted in pink. The top and leftmost panels show the cumulative f_{peak} distributions from each map. We note that these distributions are not representative of the full occurrence rates, and differ because planets may find themselves in different regions of sensitivity based on their instellation and period.

of $f(P, R_p)$ because the calculation of $f(S, R_p)$ is analogous.

The occurrence rate $f(P, R_p)$ depends on the number of recovered planets $N_p(P, R_p)$ (see Section 4) and our average survey completeness $c(P, R_p)$. We calculated the latter from the binned sensitivity maps shown in Figure 5 by weighting each map by the total number of targets therein. We note that we also tested calculating the occurrence rate map $f(P, R_p)$ using the individual sensitivity bins in Figure 5 by calculating six independent $f(P, R_p)$ maps (one for each injection–recovery bin), based on the subset of $N_p(P, R_p)$ whose host star properties fall with each bin of interest (i.e. T_{mag} and whether rotation is detected), and averaging the six maps. We confirm that our final occurrence rate inferences do not differ depending on the choice of using the average versus individual sensitivity maps.

The number of trials of each Bernoulli experiment is the number of stars searched N_* , and the number of successful experiments (i.e. planet detections) is the number of planets $N_p(P, R_p)$ found by our planet search. Dropping the function arguments P and R_p for brevity,

the posterior probability distribution for the occurrence rate f is given by

$$P(f|N_p, N_*, c) = \binom{N_*}{N_p} (fc)^{N_p} (1 - fc)^{N_* - N_p}. \quad (14)$$

It follows that the most likely value of $f(P, R_p)$ is

$$f_{\text{peak}}(P, R_p) = \frac{N_p(P, R_p)}{N_* \cdot c(P, R_p)}. \quad (15)$$

When calculating the cumulative occurrence over a large range of radii, periods, or instellations, using this method will lead to an inaccurate posterior if the survey’s completeness dynamically changes over the bins of interest. In these cases, we compute the occurrence over a log-log grid that spans the space of interest. We compute a cumulative occurrence $P(\text{Occ.} = f)$ distribution by summing samples from the grid where $N_p \geq 1$. In cases where the range of interest contains no found planets, we instead sample from all posteriors in the grid and report the average weighted by the span of each grid cell in log-log space.

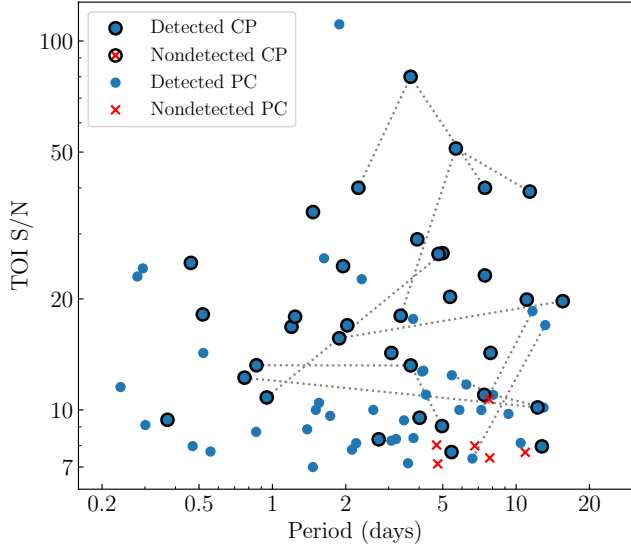


Figure 9. Detected and nondetected TOIs (as of October 2024) among stars in our survey sample as a function of orbital period and transit S/N. Detected and nondetected TOIs are depicted by circle markers and “X” markers, respectively. Confirmed planet (CP) TOIs are encircled while planet candidate (PC) TOIs are not. Known false alarms and false positives are excluded. Multiplanet systems are connected with dashed lines.

5.2. The 2D Occurrence Rate Distribution

In Table 4, we outline the occurrence rates of planets in period–radius and instellation–radius spaces with our peak occurrence rate maps $f_{\text{peak}}(P, R_p)$ and $f_{\text{peak}}(S, R_p)$ shown in Figure 8. The planetary parameters recovered in our survey are over-plotted. The panels in the top row and rightmost column of Figure 8 depict the cumulative marginalized distributions of $f_{\text{peak}}(P)$, $f_{\text{peak}}(S)$, and $f_{\text{peak}}(R_p)$, respectively. It should be noted that these distributions are not fully reflective of the cumulative planet occurrence rate as they are based solely on the most-likely occurrence rate values and do not account for the associated uncertainty in each cell.

We also highlight the regions in each panel where our average detection sensitivity is $< 10\%$. Any occurrence rate calculations over the highlighted regions of low sensitivity ($< 10\%$) are not considered reliable for computing the occurrence rate of planets. We generally planets in this region are not counted towards most of our our subsequent occurrence rate calculations, save for the ranges in Tables 4, 5 and 6 (see section 6.1), and our habitable zone planet occurrence rates. Aside from $P > 14$ days, where our sensitivity falls rapidly with increasing orbital period primarily because only 43% of our targets are searched for planets beyond 14 days (c.f. Figure 7),

the decline in our sensitivity occurs between $0.4 - 1 R_{\oplus}$ depending on the period or instellation.

One planet of note that lies in this region is Gliese 12 b ($P = 12.76$ days, $R_p = 0.95 R_{\oplus}$ M. Kuzuhara et al. 2024; S. Dholakia et al. 2024; M. Brady et al. 2025; D. A. Turner et al. 2025). This discovery has been rigorously confirmed and provides a rare example of a temperate Earth-sized planet. Our survey-averaged sensitivity to this planet falls below 10% and so we do not trust its contribution to our occurrence rate inferences, although our sensitivity to Gliese 12 b in its injection–recovery bin is $> 30\%$ due to the brightness of its host star ($T_{\text{mag}} = 10.18$) such that its detection in our survey is not unexpected.

The planetary occurrence rate calculations in Figure 8 clearly shows that the planet population around mid-to-late M dwarfs is dominated by sub- and super-Earths ($R_p \lesssim 1.6 R_{\oplus}$). With only five sub-Neptunes with $R_p \geq 2 R_{\oplus}$ in our planet sample, the occurrence rate of sub-Neptunes is less than for terrestrial bodies at all periods out to 15 days. None of our detected sub-Neptunes with $R_p > 2 R_{\oplus}$ have orbital periods within 2 days, which may suggest that such planets, that would likely harbor a large mass fraction of volatiles (i.e. H_2/He or water) on their surface, are unstable to thermally-driven atmospheric loss. We also find no planets with $R_p \geq 3 R_{\oplus}$ implying that the occurrence rates of Neptunes and gas giants, both hot and temperate, are consistent with zero⁹ around mid-to-late M dwarfs, with our upper limits across periods from 0.2-30 days outlined in Table 4. The unimodality of the $f(P, R_p)$ and $f(S, R_p)$ distributions stand in contrast to period/instellation–radius distributions around earlier type stars, specifically the occurrence rate of planets around late K to mid-M dwarfs (CM20) and the occurrence rate of planets around FGK stars (e.g B. J. Fulton et al. 2017), which both show evidence for the bimodal Radius Valley in these 2-dimensional parameter spaces.

5.3. The Planetary Radius Distribution

We derive the planetary occurrence rate as function of radius $f(R_p)$ by marginalizing $f(P, R_p)$ (c.f. Figure 8) over orbital period. Due to our low sensitivity to small planets, we only consider our cumulative radius distribution reliable for planets with $R_p > 1 R_{\oplus}$ where our average sensitivity out to 30 days is greater than 20%.

⁹ Neptunes and Jovian planets have occasionally been found around mid-to-late M dwarfs (e.g. J. M. Almenara et al. 2022; J. E. Libby-Roberts et al. 2023; S. E. Jones et al. 2024; M. G. Scott et al. 2026), none of which are in our sample of stars. We find that their occurrence rate is consistent with zero in our study, implying the rarity of these objects.

$R_p (R_\oplus)$	0.2 – 1 days	1 – 3 days	3 – 7 days	7 – 15 days	15 – 30 days
0.5 – 1.0	$0.035^{+0.014}_{-0.014}$ (19.4%)	$0.101^{+0.035}_{-0.036}$ (9.9%)	$0.343^{+0.143}_{-0.143}$ (6.1%)	$0.390^{+0.259}_{-0.239}$ (3.2%)	< 0.88 (1.2%)
1.0 – 1.5	$0.021^{+0.005}_{-0.005}$ (64.8%)	$0.141^{+0.028}_{-0.028}$ (41.9%)	$0.401^{+0.094}_{-0.094}$ (28.2%)	$0.428^{+0.140}_{-0.140}$ (17.1%)	< 0.45 (6.5%)
1.5 – 2.0	$< 9.7 \times 10^{-4}$ (91.3%)	$< 2.9 \times 10^{-3}$ (77.7%)	$0.047^{+0.017}_{-0.017}$ (60.3%)	$0.186^{+0.053}_{-0.053}$ (40.7%)	$0.058^{+0.038}_{-0.038}$ (17.0%)
2.0 – 3.0	$< 9.2 \times 10^{-4}$ (97.4%)	$< 2.2 \times 10^{-3}$ (94.1%)	$0.022^{+0.009}_{-0.009}$ (87.2%)	$0.025^{+0.012}_{-0.012}$ (67.7%)	< 0.09 (23.3%)
3.0 – 6.0	$< 9.8 \times 10^{-4}$ (99.5%)	$< 2.9 \times 10^{-3}$ (98.3%)	$< 4.8 \times 10^{-3}$ (96.8%)	$< 1.0 \times 10^{-2}$ (80.2%)	$< 6.4 \times 10^{-2}$ (28.8%)

$R_p (R_\oplus)$	$10^3 - 10^2 S_\oplus$	$10^2 - 50 S_\oplus$	$50 - 10 S_\oplus$	$10 - 5 S_\oplus$	$5 - 1 S_\oplus$
0.5 – 1.0	$0.003^{+0.002}_{-0.002}$ (23.4%)	$0.009^{+0.006}_{-0.006}$ (16.8%)	$0.176^{+0.060}_{-0.060}$ (11.1%)	$0.059^{+0.029}_{-0.029}$ (8.0%)	$0.294^{+0.196}_{-0.187}$ (5.2%)
1.0 – 1.5	$0.008^{+0.002}_{-0.002}$ (68.6%)	$0.009^{+0.003}_{-0.003}$ (55.6%)	$0.115^{+0.023}_{-0.023}$ (42.9%)	$0.173^{+0.041}_{-0.041}$ (30.8%)	$0.178^{+0.053}_{-0.053}$ (20.9%)
1.5 – 2.0	$< 9.6 \times 10^{-4}$ (91.0%)	$< 1.2 \times 10^{-3}$ (86.2%)	$0.010^{+0.005}_{-0.005}$ (77.3%)	$0.018^{+0.008}_{-0.008}$ (62.1%)	$0.141^{+0.037}_{-0.037}$ (43.6%)
2.0 – 3.0	$< 7.3 \times 10^{-4}$ (89.2%)	$< 1.5 \times 10^{-3}$ (95.8%)	$< 1.9 \times 10^{-3}$ (93.6%)	$0.019^{+0.008}_{-0.008}$ (86.4%)	$0.020^{+0.010}_{-0.010}$ (66.3%)
3.0 – 6.0	$< 7.8 \times 10^{-4}$ (90.4%)	$< 2.7 \times 10^{-3}$ (97.8%)	$< 2.2 \times 10^{-3}$ (98.3%)	$< 3.5 \times 10^{-3}$ (96.8%)	$< 8.8 \times 10^{-3}$ (73.4%)

Table 4. Top: Number of planets per star vs orbital period and planetary radius. Bottom: Number of planets per star vs instellation and planetary radius. In this table the numbers in parentheses are the target weighted percentage of all planets which were recovered in our injection–recovery tests in the given intervals.

By sampling the distributions in each cell of Figure 8 from their associated posteriors parametrized by equation 14 and integrating over orbital period, we obtain many realizations of the radius distribution of planets. We do not consider bins where $N_p = 0$ in this calculation, as samples from many distributions with non-zero tails adds an arbitrarily large amount of occurrence to the cumulative occurrence rate; however, the distributions in regions with zero occurrence can still be used to set an upper limit on the occurrence of planets therein.

We also independently estimate the underlying distribution of planets using a Gaussian kernel density estimator (KDE) with our completeness-weighted planet sample. We use the KDE to quantify the peak of the super-Earth distribution to compare the corresponding radius to the population of planets around different spectral types. We only consider planets with $R_p > 1.0 R_\oplus$ in this calculation because of the aforementioned sensitivity conditions. To determine the error on this calculation, we recompute the KDE using a bootstrapped sample with periods and radii drawn from each planet’s posterior distribution. Each planet’s sampled weight is also taken from a smooth completeness map where each injection is represented as a Gaussian width equal to one third of the width of the quadtree cell (see Figure 5) in which the injection was sampled.

These distributions of planet occurrence rates with their associated errors are shown in Figure 10. From the distribution plotted in Figure 10 it is clear that the population of planets around mid-to-late M dwarfs orbiting within 30 days is unimodal without any sign of a Radius Valley. Through our bootstrapped KDE samples,

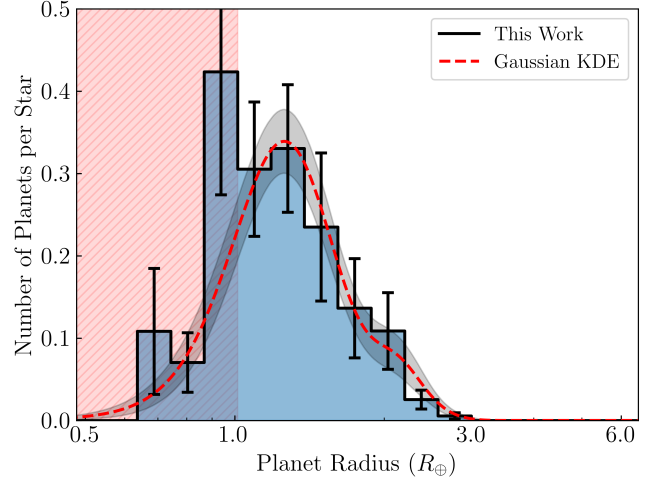


Figure 10. Occurrence rate of planets in radius space, realized by sampling the posterior distribution in each bin of Figure 8 with a Gaussian KDE of the occurrence rate overplotted. The red shaded region marks the area of low sensitivity where we consider our results unreliable.

we find that the super-Earth peak around mid-to-late M dwarfs lies at $1.25 \pm 0.05 R_\oplus$.

In Figure 11, we also compare our radius distribution to similar distributions around early-M to late-K dwarfs (CM20), and FGK stars (B. J. Fulton et al. 2017). For convenience of comparison, their super-Earth peaks are scaled to our super-Earth peak. We note that both of these surveys searched for planets out to 100 days, and we are limited to 30 days. We also note that because our sample of M stars are dimmer, the range of instellations being probed is similar. These distributions show that early M dwarfs and FGK stars have substantial popula-

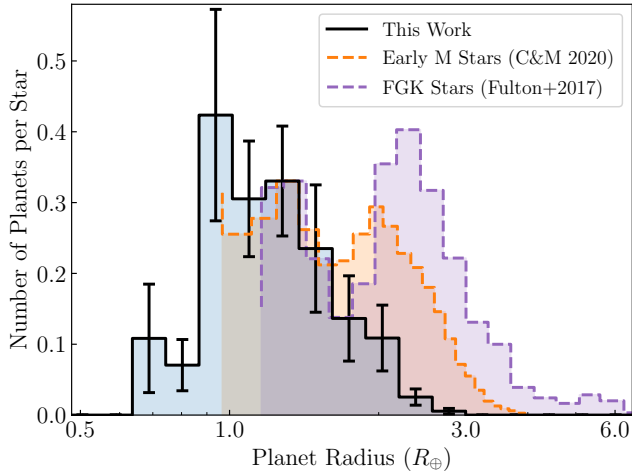


Figure 11. Comparison of our occurrence rate to the scale occurrence rates found by B. J. Fulton et al. (2017) and CM20, with each super-Earth peak scaled to match our super-Earth peak.

tions of sub-Neptunes, separated from super-Earths by a Radius Valley. Conversely, we only see a population of super-Earths, which is similarly shaped, with a sharp monotonic decline toward larger radii.

To determine the precise contributions of super-Earths and sub-Neptunes to the occurrence rate of planets around mid-to-late M dwarfs, we carry out the same binned occurrence rate calculation from 0.2–30 days over two radius ranges representing these two planet types. We find a cumulative occurrence rate of super-Earths with ($R_p = 1 - 1.6 R_\oplus$) of 0.954 ± 0.147 and a cumulative occurrence rate of sub-Neptunes with ($R_p = 1.8 - 3 R_\oplus$) of 0.148 ± 0.045 . While sub-Neptunes are represented in our sample of planets, these relative occurrence rates show that super-Earths dominate the planet population, outnumbering sub-Neptunes by a factor of 5.5 ± 1.1 to 1 around our sample of mid-to-late M dwarfs.

Without any Neptune-sized planets in our sample, we can only set an upper limit on the occurrence rate of Neptune-sized planets around mid-to-late M dwarfs. We sample the binomial distributions spanning periods from 0.2 to 30 days and radii spanning $R_p = 3 - 6.5 R_\oplus$. We find a 95th percentile upper limit to the occurrence rate of Neptunes around mid-to-late M dwarfs of ≤ 0.0341 planets per star.

5.4. The Occurrence Rate of Jovian-sized Objects

In our transit search we detect one PC outside of the radius range spanned by our injection–recovery tests. TOI-1779.01, or LP 261-75 C, for which we measure a radius of $9.7 \pm 0.3 R_\oplus$, a period of 1.88 days. This object is a known brown dwarf with a mass of $68.1 \pm 10 M_{\text{Jup}}$ (J. M. Irwin et al. 2018).

Our injection–recovery tests have not directly probed our pipeline’s sensitivity to transiting planets with $R_p > 6.5 R_\oplus$, but we can safely assume that our sensitivity to larger objects for the same orbital period is at least as good as what we calculate at the upper end of our radius range. We therefore posit that we have complete sensitivity to transiting planets with $R_p > 6.5 R_\oplus$ out to 2 days, which encapsulates the one Jovian-sized object found in our survey. Based on this single detection we measure a cumulative occurrence rate of $0.0028^{+0.0027}_{-0.0015}$ Jovian-sized objects per mid-to-late M dwarf orbiting within 10 days. Beyond this period limit our sensitivity to Jovians degrades by a factor of ~ 2 . We emphasize that this cumulative occurrence rate is of Jovian-sized objects because it is based solely on our transit survey data, which is insufficient to distinguish giant planets from sub-stellar objects.

That being said, LP 261-75 C is not truly a planet. Determining its provenance is beyond the scope of our survey and its status as a stellar companion does not invalidate our measurement of the occurrence rate of Jovian-sized objects. With this additional information however, we can place an upper limit on the occurrence rate of hot Jupiters around mid-to-late M dwarfs. Assuming that our sensitivity to hot Jupiters is at least as good as our sensitivity to $6.5 R_\oplus$ planets, we find a 95th percentile upper limit of 0.012 hot Jupiters per star orbiting within 10 days. This upper limit is consistent with the giant planet occurrence of 0.0029 ± 0.0015 around mid-to-late M dwarfs found by E. M. Bryant et al. (2023).

5.5. Occurrence of Planets within the Habitable Zone

While our sensitivity to planets in the HZ is drops off steeply beyond $\sim 1.5 S_\oplus$, we can still place constraints on the occurrence rate of planets within the habitable zone of mid-to-late M dwarfs.

We can assume empirical optimistic HZ limits of $0.2 - 2 S_\oplus$. The inner edge is bounded by the “recent Venus” scenario motivated by the inference that Venus had liquid water on its surface during its history (S. C. Solomon & J. W. Head 1991), and the outer edge emerges from the maximum greenhouse limit (R. K. Kopparapu et al. 2013). In these bounds, we find a cumulative occurrence rate of $0.178^{+0.116}_{-0.115}$ planets per star with radii between $0.4 - 6.5 R_\oplus$, and an occurrence rate of terrestrial planets between $0.8 - 1.5 R_\oplus$ of $0.142^{+0.093}_{-0.092}$ planets per star.

R. K. Kopparapu et al. (2013) provides a more conservative HZ range of $0.2 - 0.9 S_\oplus$ that corresponds to the water-loss inner edge and maximum greenhouse outer edge of the HZ. We do not find any planets in our sur-

Source		MC23	This Work
Mass range		$0.1 - 0.3M_{\odot}$	$0.1 - 0.4M_{\odot}$
Median Mass		$0.17M_{\odot}$	$0.22M_{\odot}$
Period (days)	$R_p (R_{\oplus})$	Occurrence Rate by Source	
0.2-1	0.5-4.0	$0.047^{+0.019}_{-0.015}$	0.052 ± 0.014
1-2.7		$0.159^{+0.064}_{-0.050}$	$0.175^{+0.045}_{-0.046}$
2.7-7		$0.402^{+0.162}_{-0.127}$	0.530 ± 0.099
7-30		-*	$0.510^{+0.151}_{-0.152}$
0.2-30	1.0-1.5	$0.446^{+0.162*}_{-0.118}$	$0.785^{+0.142}_{-0.144}$
	1.5-2.0	$\leq 0.073^*$	0.297 ± 0.075
	> 2.0	$\leq 0.072^*$	0.040 ± 0.013
	0.5-4.0	$0.61^{+0.24}_{-0.19*}$	$1.358^{+0.195}_{-0.195}$

Table 5. Comparison of our occurrence rate calculation in planet radius and period to [K. Ment & D. Charbonneau \(2023\)](#) (MC23). This table is an adapted version of Table 7 from [K. Ment & D. Charbonneau \(2023\)](#). *The occurrence rate calculation from [K. Ment & D. Charbonneau \(2023\)](#) extends from 0.2-7 days.

vey in this instellation range, and our sensitivity is poor, but we can still place 95th percentile upper limits on the occurrence rate of planets in this range. We find that the occurrence rate of HZ planets with radii between $0.4 - 6.5 R_{\oplus}$ is < 0.19 planets per star, and the occurrence rate of terrestrial ($0.8 - 1.5 R_{\oplus}$) habitable planets is < 0.351 planets per star. We note that this latter upper limit is larger than the former despite spanning a smaller radius range because we have poorer average sensitivity to terrestrial planets compared to all planets from $0.4 - 6.5 R_{\oplus}$. In essence, no more than 1-in-3 mid-to-late M dwarfs hosts a terrestrial planet in their habitable zone.

6. DISCUSSION

6.1. Comparison to Ment & Charbonneau 2023

The most appropriate direct comparison we can make to this occurrence rate calculation is [MC23](#) with their survey of 363 mid-to-late M dwarfs within 15 parsecs, searching for transiting planets out to 7 days. Their survey does provide constraints for the occurrence rate of super-Earths, but without any sub-Neptune detections, they could only set an upper limit on the occurrence of any second peak of the Radius Valley. By cutting the search space of our survey, we can directly compare the results of our survey to this previous occurrence rate calculation. In [Tables 5 and 6](#), we outline our relative occurrence rates.

The results of our survey are in very close agreement with the findings of [MC23](#), and the occurrence rate of

Source		MC23	This Work
Mass range		$0.1 - 0.3M_{\odot}$	$0.1 - 0.4M_{\odot}$
Median Mass		$0.17M_{\odot}$	$0.22M_{\odot}$
Instel. (S_{\oplus})	$R_p (R_{\oplus})$	Occurrence Rate by Source	
4-10	0.5-4.0	$0.303^{+0.120}_{-0.095}$	0.354 ± 0.062
10-50		$0.162^{+0.064}_{-0.051}$	0.216 ± 0.043
50-200		$0.030^{+0.012}_{-0.010}$	0.018 ± 0.006
4-200	0.5-1.0	$0.107^{+0.098}_{-0.055}$	$0.228 \pm 0.061^*$
	1.0-1.5	$0.370^{+0.162}_{-0.118}$	$0.319^{+0.056}_{-0.055}$
	1.5-2.0	≤ 0.060	0.298 ± 0.070
	> 2.0	≤ 0.056	0.044 ± 0.015
	0.5-4.0	$0.49^{+0.19}_{-0.15}$	$0.571^{+0.075}_{-0.074}$

Table 6. Comparison of our occurrence rate calculation in planet radius and instellation to [K. Ment & D. Charbonneau \(2023\)](#) (MC23). This table is an adapted version of Table 8 from [K. Ment & D. Charbonneau \(2023\)](#). *Because of our low sensitivity, we consider occurrence rates for planets $< 1R_{\oplus}$ unreliable.

sub-Neptunes lies below their lower limit. This agreement is expected, because our survey covers a very similar mass range, with our median masses differing by $0.05M_{\odot}$. Our very low sub-Neptune occurrence rate means we can confidently say that the Radius Valley disappears in this regime. Because the stars in our sample are much fainter on average than the stars surveyed by [MC23](#) we consider their work to be more reliable in constraining the population of planets with $< 1 R_{\oplus}$ out to 7 days.

6.2. Cumulative Planetary Occurrence Around Mid-to-Late M Dwarfs

We measure a cumulative occurrence rate of planets with radii $> 1 R_{\oplus}$ orbiting within 30 days of 1.10 ± 0.16 planets per star in our sample of mid-to-late M dwarfs. To put this result into context and to illustrate the trend of cumulative occurrence over a range of stellar types, we have gathered four other transit surveys, characterizing occurrence rates in main sequence stars with effective temperatures from 2700K – 7300K. [M. Kunimoto & J. M. Matthews \(2020\)](#) takes 96,280 Kepler stars and uses approximate Bayesian computation (ABC) to report the occurrence rate of planets around F ($6000\text{K} \leq T_{\text{eff}} \leq 7300\text{K}$), G ($5300\text{K} \leq T_{\text{eff}} \leq 6000\text{K}$) and K ($3900\text{K} \leq T_{\text{eff}} \leq 5300\text{K}$) type stars. [D. C. Hsu et al. \(2018\)](#) uses ABC to characterize the occurrence rate of planets around FGK type stars using the Kepler sample of planets, and [D. C. Hsu et al. \(2020\)](#) applies same methodology to planets around M stars found by Kepler. [DC15](#) searches the four-year Kepler data set

with a custom pipeline to place strong constraints on the cumulative occurrence rate of planets around a sample of M dwarfs with $2661\text{K} \leq T_{\text{eff}} \leq 3999\text{K}$ and a mean effective temperature of $3746_{-300}^{+217}\text{K}$, biasing their sample towards earlier type M stars than the stars characteristic of our sample. We also include the occurrence rate value from [MC23](#) as an upper limit because their survey only extends out to 7 days. We sample each of these surveys’ reported occurrence rates from $1 - 4 R_{\oplus}$ with $P < 30$ days to derive a cumulative occurrence that can be readily compared to our occurrence rate.

In [Figure 12](#) we illustrate these occurrence rates with their associated 1σ errors, and mark the effective temperature range that each sample spans. The mean T_{eff} is marked with a solid circle and we mark the middle T_{eff} value with a dashed circle in cases where the mean T_{eff} is not available. In general, we see an increasing trend of higher occurrence towards later stellar types, with M dwarfs, including early, mid, and late types, hosting the majority of planets larger than Earth and with periods < 30 days. Contrasting our cumulative occurrence rate of 1.10 ± 0.16 planets per star to the value around early M dwarfs (1.28 ± 0.05 ; [DC15](#)) confirms that early and mid-to-late M dwarfs host a consistent number of close-in planets larger than Earth and within 30 days. Therefore the full suite of M dwarfs that includes early, mid, and late type M dwarfs are the most prolific hosts of small close-in planets.

6.3. Comparisons to Theoretical Predictions

The TESS GI programs which secured the data used to complete our survey looked to establish the dominant driver of the Radius Valley by measuring the properties of the Radius valley around mid-to-late M dwarfs. While core-powered mass loss and photoevaporation make consistent predictions of the Radius Valley’s location and slope for Sun-like stars, the Radius Valley locations they predict diverge towards mid-to-late M dwarfs ([Y. Wu 2019](#); [A. Gupta & H. E. Schlichting 2019](#)). Our finding that the Radius Valley does not exist around mid-to-late M dwarfs prevents our survey from directly disentangling their relative effects in sculpting the Radius Valley around higher-mass stars. This being said, the non-detection of a Radius Valley in this stellar mass regime still serves to support other Radius Valley emergence models.

[R. Burn et al. \(2021\)](#) uses the Bern New Generation Planetary Population Synthesis (NGPPS) models produce populations of planets around $0.3 M_{\odot}$ and $0.1 M_{\odot}$ stars. These stellar masses overlap with stars surveyed here. Their cumulative occurrence rate of planets with periods less than 100 days is dominated by sub-Earths

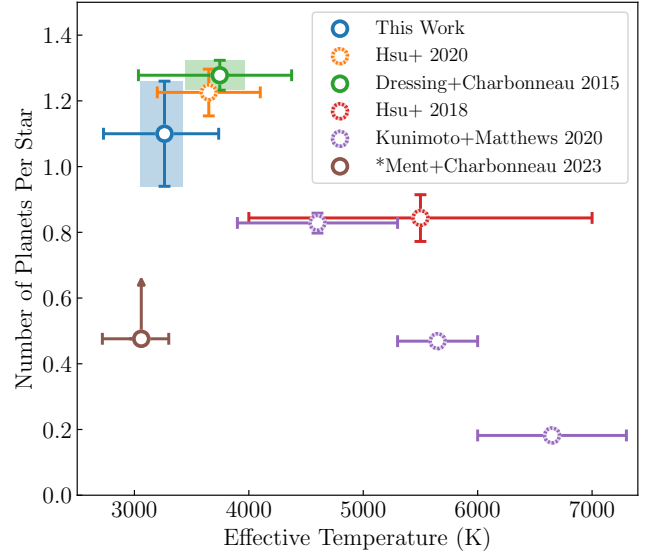


Figure 12. Cumulative occurrence rates of planets with radii spanning $1 - 4 R_{\oplus}$ and periods out to 30 days as a function of stellar effective temperature. The horizontal lines mark the recovered occurrence rate with the 1σ uncertainty in each occurrence rate calculation marked by the errorbars. The full T_{eff} range of each work is marked by the horizontal extent of each marker, and the shaded region shows the 1σ T_{eff} range in the case of this work and [DC15](#) when available. The solid markers illustrate the mean effective temperatures, while the dashed markers mark the middle effective temperature in surveys where a mean effective temperature was not available. [*MC23](#) provides an lower limit as their survey extends out to 7 days.

and Earth-mass planets ($0.5 - 2M_{\oplus}$) with very few Neptunes ($10 - 30M_{\oplus}$). 70% of $0.1 M_{\odot}$ stars and 88% $0.3 M_{\odot}$ stars host Earth-sized planets. Only 1% of their $0.1M_{\odot}$ star simulations host Neptunes, and 8% of their $0.3M_{\odot}$ stars host Neptunes. Directly comparing these populations is difficult as we are not sensitive to planet mass in our transit survey. However, their finding that sub- and super-Earths dominate the planet population is consistent with our survey, with their simulations possibly producing more of these planets. Their higher occurrence of Neptunes is a discrepancy with our results, but our median stellar mass of $0.22M_{\odot}$ and limited sensitivity to long-period planets may explain this difference. It bears noting that the Bern model’s treatment of water’s contribution to the radius of sub-Neptunes has been updated in [R. Burn et al. \(2024\)](#), which they claim is needed to replicate the Radius Valley around Sun-like stars. However, the effect of this update on their planet population around mid-to-late M dwarfs is unknown because they have not yet considered these stars in their steam simulations.

A declining population of sub-Neptunes is predicted by Y. Chachan & E. J. Lee (2023) in their work combining the theory pebble migration models with measured disk masses. They predict that as a function of disk dynamics, fewer sub-Neptunes should be expected around stars starting at $0.3\text{--}0.5M_{\odot}$. They also find that while late M disks are smaller, they have support greater pebble accretion efficiency, leading to a relatively flat occurrence rate of terrestrial planets towards smaller mass stars, which is also matched by our observations in comparison to CM20.

The results of our survey also strongly agree with the prediction from J. Venturini et al. (2024) where a Radius Valley is carved out between rocky super-Earths and water-rich, sometimes steamy sub-Neptunes. This division fades towards lower mass stars where the two planet populations overlap in planet radius. Their simulated population of planets qualitatively matches the smooth occurrence rate that we find in our survey (Figure 10), with a clear fall-off towards larger radii, with many fewer sub-Neptunes than higher mass stars. The J. Venturini et al. (2024) models suggest the Radius Valley, while clear around Sun-like stars, gets increasingly “filled in” with decreasing stellar mass as the populations of super-Earths and water-rich worlds increasingly overlap in radius space. The Radius Valley detected around early M and late K type stars (CM20) is shallower than the valley found around FGK stars (B. J. Fulton et al. 2017) and we have shown that the Radius Valley effectively disappears around mid-to-late M dwarfs. These independent transit surveys targeting different host star spectral types support the theoretical picture presented in J. Venturini et al. (2024), but deeper investigation is still necessary. If the planet population in our survey is explained by overlapping rocky and water worlds, a complete confirmation of their model’s predictions is only possible with precise mass measurements and atmospheric characterization to confirm the water-rich nature of sub-Neptunes. Both of these measurements are beyond the scope of our paper, but are well suited to observations with JWST (e.g. C. Piaulet-Ghorayeb et al. 2024).

6.4. The Observed Radius Valley

While our survey does not find a Radius Valley in this regime, we still find a peak in the super-Earth population. In comparing the population of planets across stellar types, it is useful to compare our observed population peak to the Radius Valley peaks seen around earlier type stars. Figure 11 illustrates the falloff of the sub-Neptune peak in the Radius Valley across spectral types. This progression is qualitatively consistent with

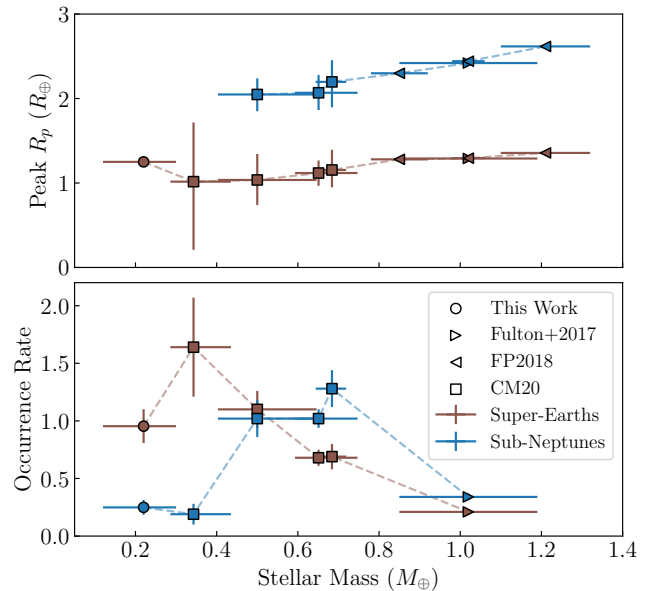


Figure 13. Evolution of the sub-Neptune and super-Earth populations across stellar mass. Top: The peak occurrence of super-Earths and sub-Neptunes plotted in brown and blue respectively. Bottom: The cumulative occurrence of super-Earths and sub-Neptunes plotted in brown and blue respectively. The data presented herein are taken from this work, F17, FP18, and CM20, and are outlined in Table 7.

the planet populations produced by water rich pebble accretion scenario in J. Venturini et al. (2024).

In Figure 13, we outline the super-Earth and sub-Neptune peaks found by B. J. Fulton & E. A. Petigura (2018) and CM20 to further compare the planet populations’ properties across stellar types. We also supply the numerical values of the peak and occurrence rates in Table 7.

Across the range of stellar masses surveyed, we consistently see the two peaks of the Radius Valley moving towards smaller radii, and moving closer together. We also see sub-Neptunes making up a smaller fraction of the planet population towards lower mass stars. This shift in the Radius Valley is overall consistent with the findings of J. Venturini et al. (2024), suggesting that water-rich worlds may play a very strong role in shaping the Radius Valley. We also find that the trend in cumulative occurrence of super-Earths and sub-Neptunes seen past $0.5M_{\odot}$ is consistent with the predictions of Y. Chachan & E. J. Lee (2023), where the observed super-Earth population is consistent with a flat line, and the sub-Neptune population drops off.

Counter to this observed trend of the super-Earth peak moving towards smaller radii, we find that the peak in our super-Earth population is higher than the peak observed by CM20. This shift of the super-Earth peak

Source	Stellar Mass (M_{\odot})	SE Peak (R_{\oplus})	SN Peak (R_{\oplus})	f_{SE} [$1R_{\oplus}, 1.6R_{\oplus}$]	f_{SN} [$1.6R_{\oplus}, 2.6R_{\oplus}$]	f_{SE}/f_{SN}
F17	1.02 ± 0.17	1.29*	2.42*	$0.21 \pm 0.02^{\dagger}$	$0.34 \pm 0.03^{\dagger}$	$0.61 \pm 0.09^{\dagger}$
FP18	1.21 ± 0.11	1.356 ± 0.007	2.617 ± 0.017	-	-	-
FP18	1.02 ± 0.04	1.294 ± 0.009	2.442 ± 0.02	-	-	-
FP18	0.85 ± 0.07	1.280 ± 0.008	2.299 ± 0.014	-	-	-
CM20	$0.684^{+0.040}_{-0.035}$	$1.154^{+0.205}_{-0.239}$	$2.197^{+0.301}_{-0.256}$	0.69 ± 0.11	1.28 ± 0.16	0.54 ± 0.11
CM20	$0.651^{+0.058}_{-0.096}$	$1.118^{+0.151}_{-0.148}$	$2.068^{+0.211}_{-0.205}$	0.68 ± 0.07	1.02 ± 0.08	0.66 ± 0.09
CM20	$0.500^{+0.097}_{-0.146}$	$1.036^{+0.297}_{-0.308}$	$2.048^{+0.191}_{-0.199}$	1.10 ± 0.16	1.02 ± 0.16	1.08 ± 0.23
CM20	$0.343^{+0.057}_{-0.092}$	$1.016^{+0.700}_{-0.807}$	-	1.64 ± 0.43	0.19 ± 0.09	8.46 ± 4.62
This Work	$0.22^{+0.10}_{-0.08}$	1.25 ± 0.05	-	$0.954^{+0.147}_{-0.146}$	$0.249^{+0.064}_{-0.064}$	3.62 ± 0.52

Table 7. Comparison of the Radius Valley peaks observed by B. J. Fulton et al. (2017), B. J. Fulton & E. A. Petigura (2018) (FP18), R. Cloutier & K. Menou (2020) (CM20) and this work over stellar masses, with 1σ ranges. *B. J. Fulton et al. (2017) values taken from their figure, $^{\dagger}f_{SE}$ and f_{SN} computed on [$1.16R_{\oplus}, 1.59R_{\oplus}$] and [$1.59R_{\oplus}, 2.7R_{\oplus}$] respectively.

towards larger radii could be a sign that our population of planets is mixed super-Earths and compact water worlds which would otherwise form the sub-Neptune peak of the Radius Valley around earlier spectral types. This being said, we do not have sufficient evidence to present this as conclusive.

7. CONCLUSIONS

In this work we have surveyed 8134 mid-to-late M dwarfs ($0.1 - 0.4 M_{\odot}$) for transiting planets using TESS with a custom built transit search pipeline. A detailed analysis of our survey’s completeness through injection–recovery tests has allowed us to characterize the planet population with radii $> 1 R_{\oplus}$ out to 30 days. Our survey comprises the deepest ever systematic search for transiting planets around mid-to-late M dwarfs. Our main findings are as follows:

1. We have confidently shown that the Radius Valley disappears around mid-to-late M dwarfs. The population of planets larger than Earth is unimodal in radius space, with a peak at $1.25 \pm 0.05 R_{\oplus}$.
2. We find that there are 0.954 ± 0.147 super-Earths ($1 - 1.6 R_{\oplus}$) and 0.148 ± 0.045 sub-Neptunes ($1.8 - 3 R_{\oplus}$) per star respectively, such that super-Earths outnumber sub-Neptunes by a factor of 5.5 ± 1.1 to 1.
3. We measure a cumulative occurrence of 1.10 ± 0.16 planets per star with radii $> 1 R_{\oplus}$. When compared to the planet populations around earlier type stars, our work shows that M dwarfs, including early, mid, and late types, are the most prolific hosts of planets larger than Earth with $P < 30$ days.

4. Our survey recovers one Jovian-sized object from which we measure a cumulative occurrence rate of $0.0028^{+0.0027}_{-0.0015}$ Jovian-sized objects per star within 10 days. Follow-up observations have shown that this object is an eclipsing brown dwarf (J. M. Irwin et al. 2018), from which we set a 95th percentile upper limit on the occurrence rate of hot Jupiters ($P < 10$ days, $R_p > 6.5 R_{\oplus}$) around mid-to-late M dwarfs of 0.012 per star.
5. We find an optimistic habitable zone ($0.2 - 2S_{\oplus}$) cumulative occurrence rate of $0.178^{+0.116}_{-0.115}$ planets per star and a terrestrial planet ($0.8 - 1.5 R_{\oplus}$) occurrence rate of $0.142^{+0.093}_{-0.092}$ planets per star. With a more conservative habitable zone ($0.2 - 0.9S_{\oplus}$), we can only place a 95th percentile upper limit on the occurrence of terrestrial HZ planets at < 0.351 per star.

ACKNOWLEDGMENTS

We acknowledge the support of the Natural Sciences and Engineering Research Council of Canada (NSERC).

This paper includes data collected with the TESS mission, obtained from the MAST data archive at the Space Telescope Science Institute (STScI). Funding for the TESS mission is provided by the NASA Explorer Program. STScI is operated by the Association of Universities for Research in Astronomy, Inc., under NASA contract NAS 5–26555. This research made use of Lightkurve, a Python package for Kepler and TESS data analysis (Lightkurve Collaboration et al. 2018). This research was enabled in part by support provided by McMaster University and the Digital Research Alliance of Canada (alliancecan.ca).

We recognize that McMaster University is located on the traditional territories of the Mississauga and Hau-

denosaunee nations, and within the lands protected by the ‘Dish with One Spoon’ wampum agreement.

REFERENCES

- Abril-Pla, O., Andreani, V., Carroll, C., et al. 2023, *PeerJ Computer Science*, 9, doi: [10.7717/peerj-cs.1516](https://doi.org/10.7717/peerj-cs.1516)
- Almenara, J. M., Bonfils, X., Forveille, T., et al. 2022, *A&A*, 667, L11, doi: [10.1051/0004-6361/202244791](https://doi.org/10.1051/0004-6361/202244791)
- Astropy Collaboration, Robitaille, T. P., Tollerud, E. J., et al. 2013, *A&A*, 558, A33, doi: [10.1051/0004-6361/201322068](https://doi.org/10.1051/0004-6361/201322068)
- Astropy Collaboration, Price-Whelan, A. M., Sipőcz, B. M., et al. 2018, *AJ*, 156, 123, doi: [10.3847/1538-3881/aabc4f](https://doi.org/10.3847/1538-3881/aabc4f)
- Astropy Collaboration, Price-Whelan, A. M., Lim, P. L., et al. 2022, *ApJ*, 935, 167, doi: [10.3847/1538-4357/ac7c74](https://doi.org/10.3847/1538-4357/ac7c74)
- Brady, M., Bean, J., Basant, R., et al. 2025, arXiv e-prints, arXiv:2506.20561, doi: [10.48550/arXiv.2506.20561](https://doi.org/10.48550/arXiv.2506.20561)
- Bryant, E. M., Bayliss, D., & Van Eylen, V. 2023, *MNRAS*, 521, 3663, doi: [10.1093/mnras/stad626](https://doi.org/10.1093/mnras/stad626)
- Burn, R., Mordasini, C., Mishra, L., et al. 2024, *Nature Astronomy*, 8, 463, doi: [10.1038/s41550-023-02183-7](https://doi.org/10.1038/s41550-023-02183-7)
- Burn, R., Schlecker, M., Mordasini, C., et al. 2021, *AAP*, 656, A72, doi: [10.1051/0004-6361/202140390](https://doi.org/10.1051/0004-6361/202140390)
- Cadieux, C., Plotnykov, M., Doyon, R., et al. 2024, *ApJL*, 960, L3, doi: [10.3847/2041-8213/ad1691](https://doi.org/10.3847/2041-8213/ad1691)
- Chachan, Y., & Lee, E. J. 2023, *ApJL*, 952, L20, doi: [10.3847/2041-8213/ace257](https://doi.org/10.3847/2041-8213/ace257)
- Chang, S. W., Byun, Y. I., & Hartman, J. D. 2015, *APJ*, 814, 35, doi: [10.1088/0004-637X/814/1/35](https://doi.org/10.1088/0004-637X/814/1/35)
- Cherubim, C., Cloutier, R., Charbonneau, D., et al. 2023, *AJ*, 165, 167, doi: [10.3847/1538-3881/acbdfc](https://doi.org/10.3847/1538-3881/acbdfc)
- Cloutier, R., & Menou, K. 2020, *The Astronomical Journal*, 159, 211, doi: [10.3847/1538-3881/ab8237](https://doi.org/10.3847/1538-3881/ab8237)
- Cloutier, R., Eastman, J. D., Rodriguez, J. E., et al. 2020, *AJ*, 160, 3, doi: [10.3847/1538-3881/ab91c2](https://doi.org/10.3847/1538-3881/ab91c2)
- Crossfield, I. J. M., Ciardi, D. R., Petigura, E. A., et al. 2016, *ApJS*, 226, 7, doi: [10.3847/0067-0049/226/1/7](https://doi.org/10.3847/0067-0049/226/1/7)
- Dholakia, S., Palethorpe, L., Venner, A., et al. 2024, *MNRAS*, 531, 1276, doi: [10.1093/mnras/stae1152](https://doi.org/10.1093/mnras/stae1152)
- Diamond-Lowe, H., Kreidberg, L., Harman, C. E., et al. 2022, *AJ*, 164, 172, doi: [10.3847/1538-3881/ac7807](https://doi.org/10.3847/1538-3881/ac7807)
- Dittmann, J. A., Irwin, J. M., Charbonneau, D., et al. 2017, *Nature*, 544, 333, doi: [10.1038/nature22055](https://doi.org/10.1038/nature22055)
- Dressing, C. D., & Charbonneau, D. 2013, *ApJ*, 767, 95, doi: [10.1088/0004-637X/767/1/95](https://doi.org/10.1088/0004-637X/767/1/95)
- Dressing, C. D., & Charbonneau, D. 2015, *APJ*, 807, 45, doi: [10.1088/0004-637X/807/1/45](https://doi.org/10.1088/0004-637X/807/1/45)
- Evans, D. W., Riello, M., De Angeli, F., et al. 2018, *A&A*, 616, A4, doi: [10.1051/0004-6361/201832756](https://doi.org/10.1051/0004-6361/201832756)
- Foreman-Mackey, D. 2018, *Research Notes of the American Astronomical Society*, 2, 31, doi: [10.3847/2515-5172/aaaf6c](https://doi.org/10.3847/2515-5172/aaaf6c)
- Foreman-Mackey, D., Hogg, D. W., Lang, D., & Goodman, J. 2013, *PASP*, 125, 306, doi: [10.1086/670067](https://doi.org/10.1086/670067)
- Fulton, B. J., & Petigura, E. A. 2018, *AJ*, 156, 264, doi: [10.3847/1538-3881/aae828](https://doi.org/10.3847/1538-3881/aae828)
- Fulton, B. J., Petigura, E. A., Howard, A. W., et al. 2017, *The Astronomical Journal*, 154, 109, doi: [10.3847/1538-3881/aa80eb](https://doi.org/10.3847/1538-3881/aa80eb)
- Gaidos, E., Ali, A., Kraus, A. L., & Rowe, J. F. 2024, *MNRAS*, 534, 3277, doi: [10.1093/mnras/stae2207](https://doi.org/10.1093/mnras/stae2207)
- Garcia, L. J., Foreman-Mackey, D., Murray, C. A., et al. 2024, *Astronomy Journals*, 167, 284, doi: [10.3847/1538-3881/ad3cd6](https://doi.org/10.3847/1538-3881/ad3cd6)
- Giacalone, S., & Dressing, C. D. 2020, <http://ascl.net/2002.004>
- Giacalone, S., Dressing, C. D., Jensen, E. L. N., et al. 2021, *Astronomy Journals*, 161, 24, doi: [10.3847/1538-3881/abc6af](https://doi.org/10.3847/1538-3881/abc6af)
- Gillon, M., Triaud, A. H. M. J., Demory, B.-O., et al. 2017, *Nature*, 542, 456, doi: [10.1038/nature21360](https://doi.org/10.1038/nature21360)
- Gupta, A., & Schlichting, H. E. 2019, *Monthly Notices of the Royal Astronomical Society*, 487, 24, doi: [10.1093/mnras/stz1230](https://doi.org/10.1093/mnras/stz1230)
- Hardegree-Ullman, K. K., Cushing, M. C., Muirhead, P. S., & Christiansen, J. L. 2019, *AJ*, 158, 75, doi: [10.3847/1538-3881/ab21d2](https://doi.org/10.3847/1538-3881/ab21d2)
- Hardegree-Ullman, K. K., Bergsten, G. J., Christiansen, J. L., et al. 2025, *AJ*, 170, 183, doi: [10.3847/1538-3881/adff633](https://doi.org/10.3847/1538-3881/adff633)
- Harris, C. R., Millman, K. J., van der Walt, S. J., et al. 2020, *Nature*, 585, 357, doi: [10.1038/s41586-020-2649-2](https://doi.org/10.1038/s41586-020-2649-2)
- Hippke, M., & Heller, R. 2019a, *A&A*, 623, A39, doi: [10.1051/0004-6361/201834672](https://doi.org/10.1051/0004-6361/201834672)
- Hippke, M., & Heller, R. 2019b, *Astrophysics Source Code Library*, record ascl:1910.007
- Ho, C. S. K., Rogers, J. G., Van Eylen, V., Owen, J. E., & Schlichting, H. E. 2024, *MNRAS*, 531, 3698, doi: [10.1093/mnras/stae1376](https://doi.org/10.1093/mnras/stae1376)
- Howard, A. W., Marcy, G. W., Bryson, S. T., et al. 2012, *ApJS*, 201, 15, doi: [10.1088/0067-0049/201/2/15](https://doi.org/10.1088/0067-0049/201/2/15)
- Hsu, D. C., Ford, E. B., Ragozzine, D., & Morehead, R. C. 2018, *AJ*, 155, 205, doi: [10.3847/1538-3881/aab9a8](https://doi.org/10.3847/1538-3881/aab9a8)

- Hsu, D. C., Ford, E. B., & Terrien, R. 2020, *MNRAS*, 498, 2249, doi: [10.1093/mnras/staa2391](https://doi.org/10.1093/mnras/staa2391)
- Irwin, J. M., Charbonneau, D., Esquerdo, G. A., et al. 2018, *AJ*, 156, 140, doi: [10.3847/1538-3881/aad9a3](https://doi.org/10.3847/1538-3881/aad9a3)
- Jenkins, J. M. 2002, *ApJ*, 575, 493, doi: [10.1086/341136](https://doi.org/10.1086/341136)
- Jenkins, J. M., Chandrasekaran, H., McCauliff, S. D., et al. 2010, in *Society of Photo-Optical Instrumentation Engineers (SPIE) Conference Series*, Vol. 7740, *Software and Cyberinfrastructure for Astronomy*, ed. N. M. Radziwill & A. Bridger, 77400D, doi: [10.1117/12.856764](https://doi.org/10.1117/12.856764)
- Jones, S. E., Stefánsson, G., Masuda, K., et al. 2024, *AJ*, 168, 93, doi: [10.3847/1538-3881/ad55ea](https://doi.org/10.3847/1538-3881/ad55ea)
- Koch, D. G., Borucki, W. J., Basri, G., et al. 2010, *APJL*, 713, L79, doi: [10.1088/2041-8205/713/2/L79](https://doi.org/10.1088/2041-8205/713/2/L79)
- Kopparapu, R. K., Ramirez, R., Kasting, J. F., et al. 2013, *ApJ*, 765, 131, doi: [10.1088/0004-637X/765/2/131](https://doi.org/10.1088/0004-637X/765/2/131)
- Kovács, G., Zucker, S., & Mazeh, T. 2002, *AAP*, 391, 369, doi: [10.1051/0004-6361:20020802](https://doi.org/10.1051/0004-6361:20020802)
- Kreidberg, L. 2015, *PASP*, 127, 1161, doi: [10.1086/683602](https://doi.org/10.1086/683602)
- Kunimoto, M., & Matthews, J. M. 2020, *AJ*, 159, 248, doi: [10.3847/1538-3881/ab88b0](https://doi.org/10.3847/1538-3881/ab88b0)
- Kuzuhara, M., Fukui, A., Livingston, J. H., et al. 2024, *ApJL*, 967, L21, doi: [10.3847/2041-8213/ad3642](https://doi.org/10.3847/2041-8213/ad3642)
- Libby-Roberts, J. E., Schutte, M., Hebb, L., et al. 2023, *AJ*, 165, 249, doi: [10.3847/1538-3881/accc2f](https://doi.org/10.3847/1538-3881/accc2f)
- Lightkurve Collaboration, Cardoso, J. V. d. M., Hedges, C., et al. 2018,, *Astrophysics Source Code Library* <http://ascl.net/1812.013>
- Luque, R., & Pallé, E. 2022, *Science*, 377, 1211, doi: [10.1126/science.abl7164](https://doi.org/10.1126/science.abl7164)
- Mann, A. W., Feiden, G. A., Gaidos, E., Boyajian, T., & von Braun, K. 2015, *ApJ*, 804, 64, doi: [10.1088/0004-637X/804/1/64](https://doi.org/10.1088/0004-637X/804/1/64)
- Mann, A. W., Dupuy, T., Kraus, A. L., et al. 2019, *ApJ*, 871, 63, doi: [10.3847/1538-4357/aaf3bc](https://doi.org/10.3847/1538-4357/aaf3bc)
- Mann, A. W., Wood, M. L., Schmidt, S. P., et al. 2022, *AJ*, 163, 156, doi: [10.3847/1538-3881/ac511d](https://doi.org/10.3847/1538-3881/ac511d)
- Ment, K., & Charbonneau, D. 2023, *The Astronomical Journal*, 165, 265, doi: [10.3847/1538-3881/acd175](https://doi.org/10.3847/1538-3881/acd175)
- Ment, K., Dittmann, J. A., Astudillo-Defru, N., et al. 2019, *AJ*, 157, 32, doi: [10.3847/1538-3881/aaf1b1](https://doi.org/10.3847/1538-3881/aaf1b1)
- Mullally, S., et al. 2025 <https://exovetter.readthedocs.io/en/latest/>
- Owen, J. E., & Wu, Y. 2017, *The Astrophysical Journal*, 847, 29, doi: [10.3847/1538-4357/aa890a](https://doi.org/10.3847/1538-4357/aa890a)
- Pecaut, M. J., & Mamajek, E. E. 2013, *ApJS*, 208, 9, doi: [10.1088/0067-0049/208/1/9](https://doi.org/10.1088/0067-0049/208/1/9)
- Piaulet, C., Benneke, B., Almenara, J. M., et al. 2023, *Nature Astronomy*, 7, 206, doi: [10.1038/s41550-022-01835-4](https://doi.org/10.1038/s41550-022-01835-4)
- Piaulet-Ghorayeb, C., Benneke, B., Radica, M., et al. 2024, *ApJL*, 974, L10, doi: [10.3847/2041-8213/ad6f00](https://doi.org/10.3847/2041-8213/ad6f00)
- Reid, I. N., & Walkowicz, L. M. 2006, *PASP*, 118, 671, doi: [10.1086/503446](https://doi.org/10.1086/503446)
- Ricker, G. R., Winn, J. N., Vanderspek, R., et al. 2015, *Journal of Astronomical Telescopes, Instruments, and Systems*, 1, 014003, doi: [10.1117/1.JATIS.1.1.014003](https://doi.org/10.1117/1.JATIS.1.1.014003)
- Schröter, S., Czesla, S., & Zechmeister, M. 2019, <https://github.com/sczesla/PyAstronomy/blob/master/src/pyTiming/pyPeriod/gls.py>
- Scott, M. G., Dransfield, G., Timmermans, M., et al. 2026, *MNRAS*, doi: [10.1093/mnras/stag070](https://doi.org/10.1093/mnras/stag070)
- Smith, J. C., Stumpe, M. C., Van Cleve, J. E., et al. 2012, *PASP*, 124, 1000, doi: [10.1086/667697](https://doi.org/10.1086/667697)
- Solomon, S. C., & Head, J. W. 1991, *Science*, 252, 252, doi: [10.1126/science.252.5003.252](https://doi.org/10.1126/science.252.5003.252)
- Stumpe, M. C., Smith, J. C., Catanzarite, J. H., et al. 2014, *PASP*, 126, 100, doi: [10.1086/674989](https://doi.org/10.1086/674989)
- Stumpe, M. C., Smith, J. C., Van Cleve, J. E., et al. 2012, *PASP*, 124, 985, doi: [10.1086/667698](https://doi.org/10.1086/667698)
- Sullivan, P. W., Winn, J. N., Berta-Thompson, Z. K., et al. 2017, *ApJ*, 837, 99, doi: [10.3847/1538-4357/837/1/99](https://doi.org/10.3847/1538-4357/837/1/99)
- Torres, G., Kane, S. R., Rowe, J. F., et al. 2017, *AJ*, 154, 264, doi: [10.3847/1538-3881/aa984b](https://doi.org/10.3847/1538-3881/aa984b)
- Turner, D. A., Eschen, Y. N. E., Murgas, F., et al. 2025, *arXiv e-prints*, arXiv:2506.20564, doi: [10.48550/arXiv.2506.20564](https://doi.org/10.48550/arXiv.2506.20564)
- Twicken, J. D., Jenkins, J. M., Caldwell, D. A., et al. 2025, *Research Notes of the American Astronomical Society*, 9, 132, doi: [10.3847/2515-5172/addec4](https://doi.org/10.3847/2515-5172/addec4)
- Venturini, J., Ronco, M. P., Guilera, O. M., et al. 2024, *AAP*, 686, L9, doi: [10.1051/0004-6361/202349088](https://doi.org/10.1051/0004-6361/202349088)
- Virtanen, P., Gommers, R., Oliphant, T. E., et al. 2020, *Nature Methods*, 17, 261, doi: [10.1038/s41592-019-0686-2](https://doi.org/10.1038/s41592-019-0686-2)
- Winters, J. G., Henry, T. J., Lurie, J. C., et al. 2015, *The Astronomical Journal*, 149, 5, doi: [10.1088/0004-6256/149/1/5](https://doi.org/10.1088/0004-6256/149/1/5)
- Wu, Y. 2019, *The Astrophysical Journal*, 874, 91, doi: [10.3847/1538-4357/ab06f8](https://doi.org/10.3847/1538-4357/ab06f8)

APPENDIX

A. FULL PLANET PARAMETERS

Table 8 presents a shortened version of the the full set of planetary and stellar parameters for the PCs detected by our survey. A full version of this table is available in machine-readable form.

TIC	TOI	Period (days)	Instel. (S_{\oplus})	Radius (R_{\oplus})	b	S/N	T_{mag}	M_{\star} (M_{\oplus})	R_{\star} (R_{\oplus})	T_{eff} (K)
18318288	6086.01	$1.3888677^{+0.0000051}_{-0.0000046}$	$29.2^{+2.8}_{-2.6}$	$1.11^{+0.07}_{-0.08}$	$0.46^{+0.13}_{-0.19}$	7.89	12.41	$0.23^{+0.01}_{-0.01}$	$0.26^{+0.01}_{-0.01}$	3232^{+49}_{-50}
22233480	4438.01	$7.446291^{+0.0000204}_{-0.0000223}$	$5.9^{+0.5}_{-0.5}$	$2.49^{+0.08}_{-0.08}$	$0.16^{+0.12}_{-0.11}$	18.55	11.27	$0.36^{+0.02}_{-0.02}$	$0.38^{+0.01}_{-0.01}$	3387^{+50}_{-50}
34986694	6717.01	$0.4707468^{+0.0000010}_{-0.0000011}$	$97.6^{+9.6}_{-8.8}$	$1.46^{+0.14}_{-0.13}$	$0.58^{+0.16}_{-0.22}$	9.28	13.91	$0.19^{+0.01}_{-0.01}$	$0.22^{+0.01}_{-0.01}$	3189^{+49}_{-50}
36724087	732.01	$0.7683797^{+0.0000003}_{-0.0000003}$	$120.8^{+11.2}_{-10.4}$	$1.27^{+0.05}_{-0.05}$	$0.49^{+0.07}_{-0.08}$	16.68	10.58	$0.36^{+0.02}_{-0.02}$	$0.37^{+0.01}_{-0.01}$	3387^{+51}_{-50}
36724087	732.02	$12.2522405^{+0.0000148}_{-0.0000147}$	$3.0^{+0.3}_{-0.3}$	$2.0^{+0.09}_{-0.09}$	$0.79^{+0.02}_{-0.02}$	10.85	10.58	$0.36^{+0.02}_{-0.02}$	$0.37^{+0.01}_{-0.01}$	3387^{+51}_{-50}

Table 8. Parameters of the 77 planet candidates found by this survey. The complete table is available as a csv file in the arXiv source code.

B. TIC 149927512 PLANET CANDIDATE

Our planet search finds one transit-like signal not associated with a confirmed planet, TOI, or CTOI around TIC 149927512 ($M_{\star} = 0.25 M_{\odot}$, $R_{\star} = 0.27 R_{\odot}$, $T_{\text{eff}} = 3269$ K) with an orbital period of $P = 1.4646834^{+0.0000028}_{-0.0000024}$ days and a radius of $R_p = 0.917^{+0.070}_{-0.067} R_{\oplus}$. In this appendix, we present the in-transit centroid offsets, TLS results, PDCSAP light curves, phase-folded light curve with fitted transit model, and transiting planet parameters of this PC. These figures are intended for diagnostic purposes.

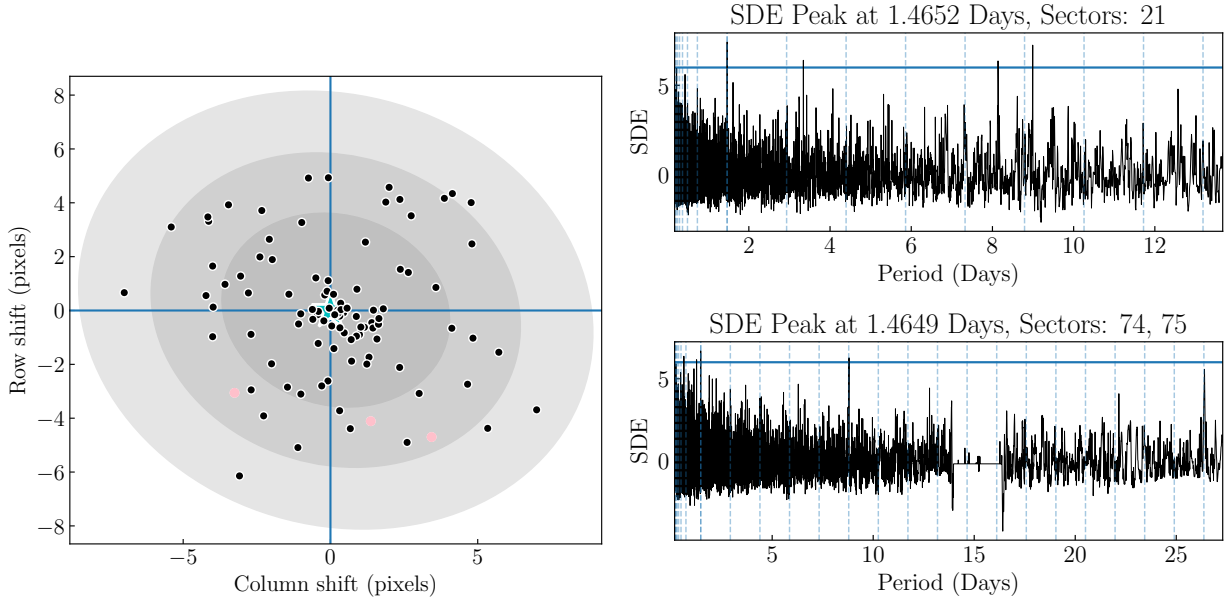


Figure 14. Left: In-transit centroid offsets of each of the 84 transit events observed. The star marker marks the out-of-transit centroid and the black points mark the relative in-transit centroid positions. We see no evidence of a systematic offset, but note that the shallow individual transit depths mean that some transits may have weakly constrained in-transit centroids, which drives the large scatter in centroid offsets of ~ 4 pixels. Right: TLS SDE spectra from the light curves where this planet candidate was detected (i.e. sectors 21 and the combined sectors 74, 75). The solid blue lines mark our SDE cutoff of 6 and the dashed lines mark harmonics of the most-likely orbital period of 1.46 days.

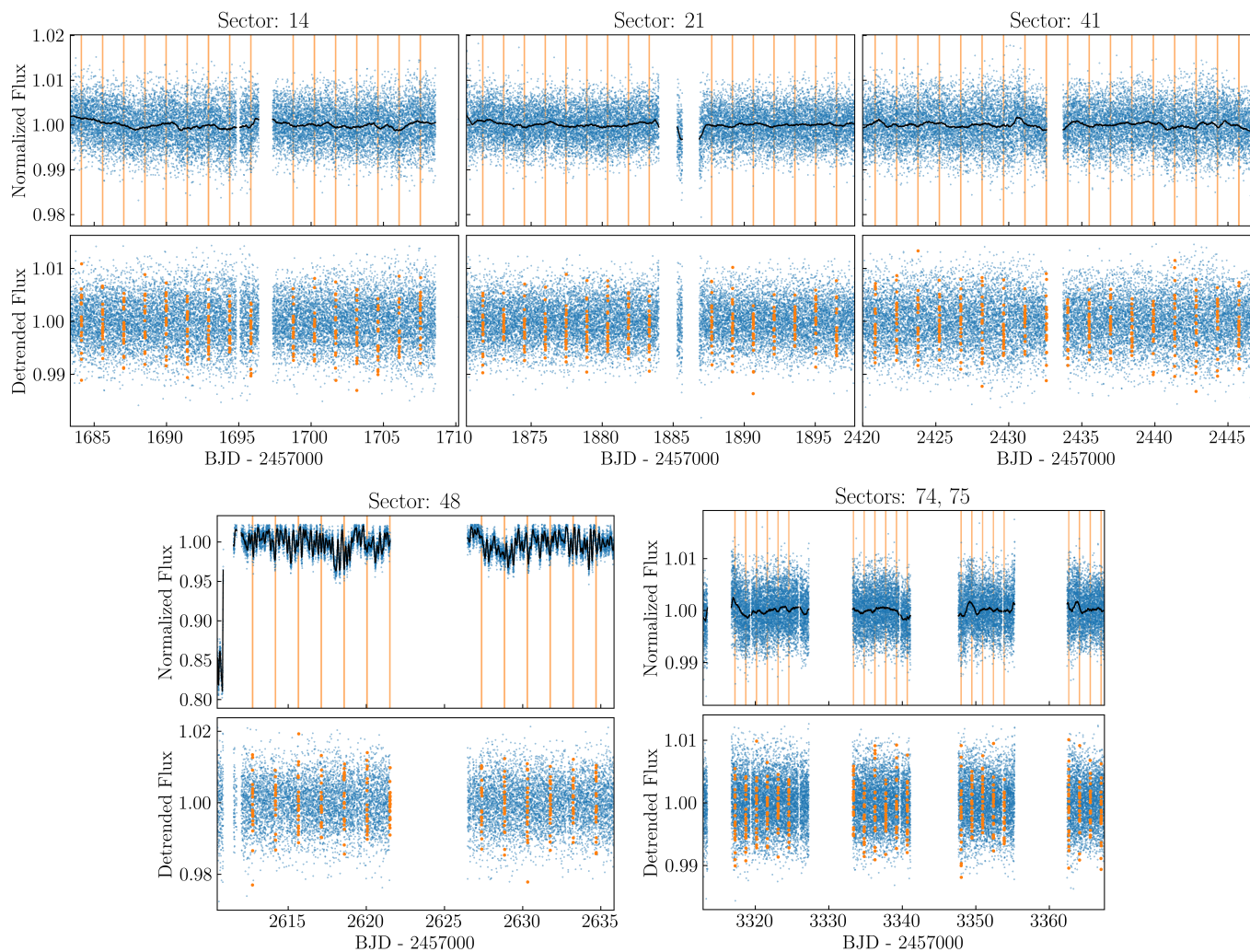


Figure 15. Pre-detrending (top) and post-detrending (bottom) PDCSAP light curves of TIC 149927512 in each of TESS sector of observation. In-transit points are highlighted in orange and the black curves represent the median detrending models in each light curve.

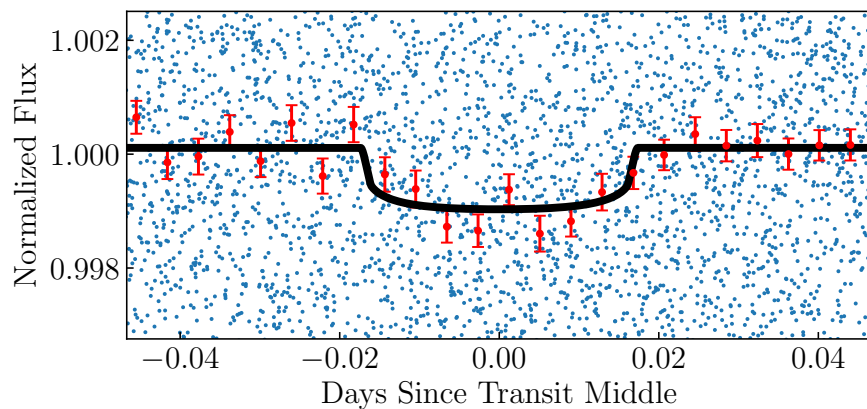


Figure 16. The detrended light curve of TIC 149927512 phase-folded to the ephemeris of the planet candidate. The binned light curve is shown in red with our best-fit transit model in black. This fit has a transit S/N of 8.03.

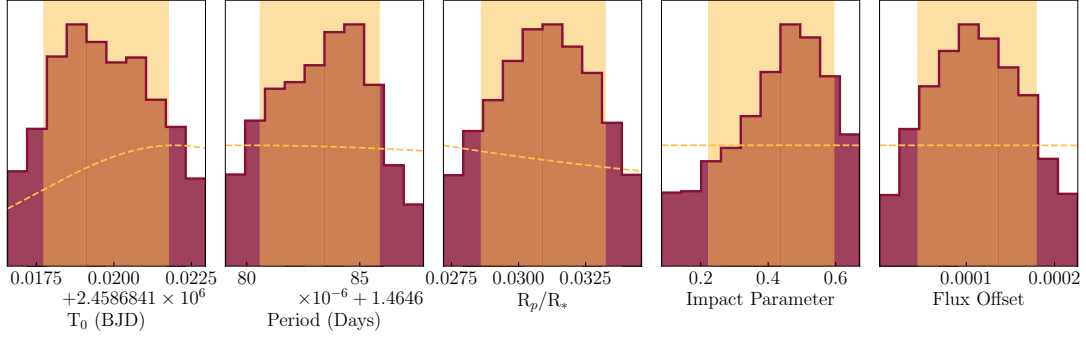


Figure 17. Posterior distributions for the parameters fit by our transit model. 1σ confidence intervals are highlighted in orange, with each parameter’s prior distribution marked by the dashed line.

Facilities: Transiting Exoplanet Survey Satellite (TESS; G. R. Ricker et al. 2015).

Software: `astropy` (Astropy Collaboration et al. 2013, 2018, 2022), `celerite2` (D. Foreman-Mackey 2018), `batman` (L. Kreidberg 2015), `emcee` (D. Foreman-Mackey et al. 2013), `exovetter` (S. Mullally et al. 2025), `GLS` (S. Schröter et al. 2019), `lightkurve` (Lightkurve Collaboration et al. 2018), `numpy`, (C. R. Harris et al. 2020), `PyMC`, (O. Abril-Pla et al. 2023), `scipy` (P. Virtanen et al. 2020), `TLS` (M. Hippke & R. Heller 2019a,b), `TRICERATOPS` (S. Giacalone & C. D. Dressing 2020; S. Giacalone et al. 2021)